Comparative Evaluation of Cast Aluminum Alloys for Automotive Cylinder Heads: Part II—Mechanical and Thermal Properties

SHIBAYAN ROY, LAWRENCE F. ALLARD, ANDRES RODRIGUEZ, WALLACE D. PORTER, and AMIT SHYAM

The first part of this study documented the as-aged microstructure of five cast aluminum alloys namely, 206, 319, 356, A356, and A356 + 0.5Cu, that are used for manufacturing automotive cylinder heads (Roy *et al.* in Metall Mater Trans A, 2016). In the present part, we report the mechanical response of these alloys after they have been subjected to various levels of thermal exposure. In addition, the thermophysical properties of these alloys are also reported over a wide temperature range. The hardness variation due to extended thermal exposure is related to the evolution of the nano-scale strengthening precipitates for different alloy systems (Al-Cu, Al-Si-Cu, and Al-Si). The effect of strengthening precipitates (size and number density) on the mechanical response is most obvious in the as-aged condition, which is quantitatively demonstrated by implementing a strength model. Significant coarsening of precipitates from long-term heat treatment removes the strengthening efficiency of the nano-scale precipitates for all these alloys systems. Thermal conductivity of the alloys evolve in an inverse manner with precipitate coarsening compared to the strength, and the implications of the same for the durability of cylinder heads are noted.

I. INTRODUCTION

IN the first part of this two part publication,[1] a detailed description of the as-aged microstructure of several cast aluminum alloys (206, 319, 356, A356, and A356 + 0.5Cu) for cylinder head application was provided. The present part deals with the mechanical and thermal properties of these alloys under different heat treatment schedules. Besides their historical role in the discovery of precipitation and age hardening,[2–4] the Al-Cu alloys has primarily been studied as a model system to understand various fundamental characteristics of nano-scale metastable precipitates (Gunier-Preston Zone or GPI, θ'' and θ'). For examples, previous studies have outlined the structure of these precipitates and their mechanism of formation using high-resolution transmission electron microscopy (HRTEM)[5–7] and also through atom probe tomography.[8–10] Clustering along with early-stage nucleation phenomena[11] and various possible orientation relationships with the α-Al matrix have also been investigated.[12]

Several studies were conducted to determine the precipitate–matrix interfacial energy[13–15] as well as the equilibrium shape and thickness of these metastable precipitates[16–18] and their coarsening behavior with heat treatment.[19–21] Another useful aspect of the reported studies on Al-Cu alloys is in the development of strength models or process models which are effective ways to quantitatively couple the structural parameters (on different length scales) to the mechanical response of precipitate hardened systems.[22–25] As for the Al-Si-Cu alloys with the same metastable GPI, θ'' and θ' precipitates, previous studies have elucidated their aging kinetics and effect of heat treatment, composition (Mg addition, Sr modification), grain refinement, *etc.*, on the aging behavior.[26–29] The strength and process models have also been developed for Al-Si-Cu alloys.[30]

Limited number of studies when compared to the nano-scale precipitates, but the effect of micrometer size ranged intermetallic precipitates for Al-Cu (A206)[31,32] has also been reported. For the Al-Si-Cu alloys, several reports are available that describe the effect of various micro-alloying element additions (Cr, Ti, Zr, V, La, Gd, *etc.*),[33–38] aging and heat treatment condition,[38,39] solidification conditions,[40] major alloying elements (Fe, Mg, Sr) addition,[38,41,42] *etc.*, on their mechanical response. Either the alloying additions or the alteration of heat treatment conditions affect the relevant mechanical properties through the formation of various intermetallic compounds or by the modification of eutectic Si particles.

The characteristics of several of the nano-scale strengthening precipitates (β'' and β'-MgSi$_2$) have also been reported for Al-Si alloys.[43] Precipitation sequence

SHIBAYAN ROY is with the Materials Science and Technology Division, Oak Ridge National Laboratory, Oak Ridge, TN 37831, and also with the Materials Science Centre, Indian Institute of Technology, Kharagpur 721302, India, Contact e-mail: shibayan@msc.iitkgp.ernet.in; royshiba@gmail.com LAWRENCE F. ALLARD, WALLACE D. PORTER, and AMIT SHYAM are with the Materials Science and Technology Division, Oak Ridge National Laboratory. ANDRES RODRIGUEZ is with Nemak, S.A., 66000 García, N.L., Mexico.
Manuscript submitted May 18, 2016.
Article published online March 8, 2017.

and structural transformation of these nano-scale precipitates have been investigated using HRTEM.[44–48] Composition and early-stage clustering of such precipitates were also determined using atom probe tomography.[49] Several studies have reported the effect of solidification,[50] heat treatment conditions,[51] and alloying (Cu, P, Y, Sr, *etc.*) [52–55] on the formation of the coarse intermetallic in these alloys while the subsequent effect of such microstructural features on the mechanical response of castings has also been evaluated.[56] The dissolution of these coarse intermetallic precipitates and subsequent nano-scale precipitation on heat treatment was also studied.[57] Finally, aging kinetics and age hardening behavior of Al-Si-Mg alloys has been reported in great detail as a function of aging heat treatment parameters[58,59] and composition, particularly Mg[60] and Si-content.[61] Similar to the Al-Cu alloys, the age hardening response of Al-Si-Cu or Al-Si alloys has also been explored to develop strength models for rod-shaped β'-Mg_2Si precipitates.[62–65]

As has been outlined in the first part, the present study aims to develop a comprehensive evaluation of five common aluminum cast alloys used for automotive cylinder heads (206-T6, 319-T7, 356-T6, A356-T6, and A356 + 0.5Cu-T6). To the best knowledge of the authors, there is no comparative study illustrating the similarities and differences in the aging response of these cast alloy systems. Also rare is any systematic effort to report the long-term thermal stability of the strengthening precipitates and corresponding contribution toward the strength of these alloys. These two aspects form the basis of the present study wherein the mechanical response of these five alloys is compared during isothermal aging and isochronal pre-conditioning heat treatments. The differences between the alloy systems (Al-Cu *vs* Al-Si-Cu *vs* Al-Si) are then realized by implementing strength models that help couple the microstructural features to the corresponding mechanical response. A comparative report of the thermal properties (specific heat, thermal diffusivity, and conductivity) of these five alloys is also performed in the present manuscript. Finally, we demonstrate that the evolution of the precipitates due to sustained elevated temperature exposure has beneficial effects on thermal conductivity but detrimental effects on strength. Understanding the microstructure-dependent competition between thermal and mechanical properties is relevant for developing new alloys with improved elevated temperature performance.

II. EXPERIMENTAL PROCEDURE

A. *Materials and Heat Treatment*

The details of the cast alloy compositions and heat treatment schedule (solution treatment and aging) are provided in Section II–A of Part I. Also the pre-conditioning treatment of the as-aged alloys was mentioned, which corresponds to an extended heat treatment at designated temperatures 473 K (200 °C), 523 K (250 °C), and 573 K (300 °C) for 200 hours. For the present part of the study, the heat-treated alloy blanks were used for various mechanical and thermal characterizations. For the reader's benefit, the alloy compositions are reproduced as in Table I from Part I (Table I). In addition, the solution and aging treatment is given in Table II (originally Table II from Part I) for the five investigated alloys.

B. *Electron Microscopy and Image Analysis for Nano-structure Characterization*

Experimental details on the characterization of nano-scale precipitates in various alloys (206, 319 and A356) by (scanning) transmission electron microscope (STEM) are reported in Section II–C of Part I. This includes the details about specimen preparation and imaging conditions.

Table I. Detailed Compositions (in Wt Pct) of Various Alloys (Only the Major Alloying Elements are Mentioned, Minor Elements in ppm Level Includes Pb, Na, Sr, P, B, Ca *etc.*)

Alloy-Condition	Si	Cu	Fe	Mn	Mg	Zn	Ti	Al (Balance)
206	0.17	5	0.15	0.25	0.32	0.005	0.021	93.88
319	8.3	3.17	0.68	0.39	0.34	0.31	0.1	86.62
356	7.21	0.14	0.39	0.25	0.37	0.17	0.19	91.28
A356	7.32	0.01	0.18	0.06	0.4	0.005	0.16	91.87
A356 + 0.5Cu	7.46	0.44	0.14	0.08	0.34	0.01	0.16	91.37

Table II. Solution Treatment and Subsequent Aging Conditions for Various Alloys

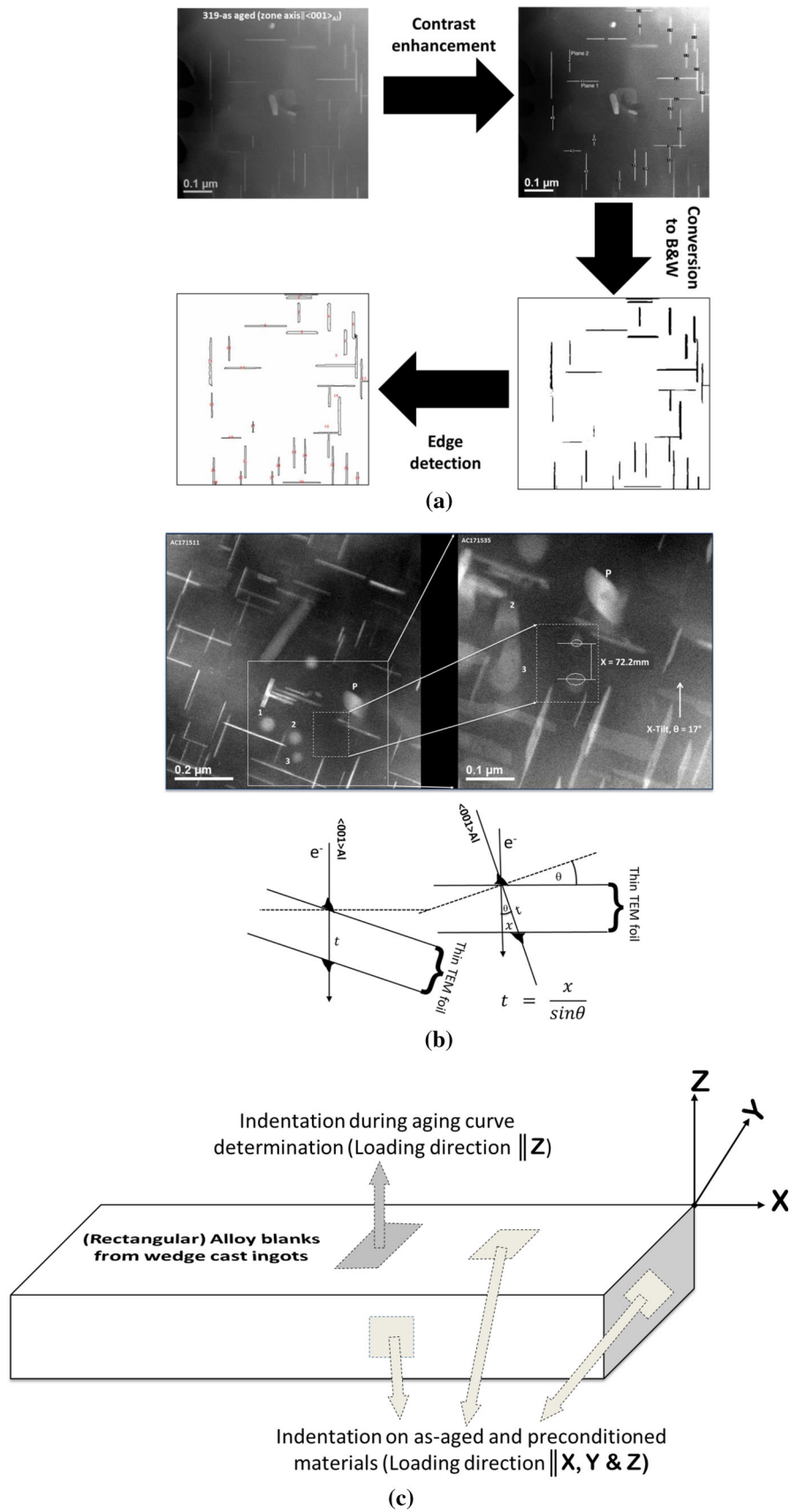| Alloy	Temper Designation	Solution Treatment Condition	Aging Conditions
206	T6	803 K (530 °C) for 5 h	463 K (190 °C) for 5 h
319	T7	763 K (490 °C) for 5 h	513 K (240 °C) for 5 h
356	T6	783 K (510 °C) for 5 h	483 K (210 °C) for 5 h
A356	T6	803 K (530 °C) for 5 h	433 K (160 °C) for 5 h
A356 + 0.5Cu	T6	803 K (530 °C) for 5 h	433 K (160 °C) for 5 h

(a)

(b)

(c)

Fig. 1—(*a*) Series of steps followed for image analysis of HAADF-STEM micrographs, (*b*) measurement scheme for TEM foil thickness (both shown for 319 alloy) and (*c*) schematic showing the scheme of mechanical characterization *via* indention.

The nano-scale precipitates in Al-Cu (206) and Al-Si-Cu (319) alloys (plate-shaped θ'' or θ' and Al-Si (A356) alloy (rod-shaped β') were imaged with $\langle 001 \rangle_{Al}$ zone axis for image analysis. This is shown in Figure 1(a) for the θ' precipitates in the 319 alloy where the STEM image is the same as the image originally shown in Figure 9(b) of Part I. The raw image was first digitally enhanced for adequate contrast difference between the precipitate and the α-Al matrix. The image was then binarized such that only the precipitates become visible as black features in a white background of the matrix. Finally, the inbuilt edge detection algorithm in ImageJ®* was applied to accurately

*ImageJ® developed by National Institute of Health, USA

determine the boundary between the precipitate and the matrix. The dimensions (length and width) of the precipitates were determined through a linear intercept method using several vertical and horizontal lines. Weighted average and the corresponding error values were calculated from the cumulative distribution of these linear intercepts with 95 pct confidence interval. Number density and area fraction of these precipitates were determined from the measured count and total area of imaging.

For strength modeling, it was further needed to measure the TEM foil thickness along the $\langle 001 \rangle_{\alpha\text{-Al}}$ zone axis for the three alloys, for areas used for determination of the dimensions of the precipitates. TEM foil thicknesses were determined using a simple contamination spot technique, as explained elsewhere.[66] In the example shown in Figure 1(b) for the 319 alloy, several trial carbonaceous contamination spots (labeled 1, 2, 3) were first created on the TEM foil surface with the electron beam in a precise $\langle 001 \rangle_{\alpha\text{-Al}}$ zone axis orientation. The inset square shows the area for analysis of thickness, in the second image of Figure 1(b). The smaller dotted rectangle indicates the area on the Al matrix for the deposition of a small contamination spot (spots actually form on both foil surfaces during this process). Precipitate particle P is also indicated, to orient the view. Afterward, the TEM specimen holder was tilted by a pre-defined angle ($\theta = 17$ deg for the present case) with respect to the x-axis (indicated in Figure). The distance between two of these spots is now measured (x). From simple geometrical considerations, the TEM foil thickness (t) in the beam direction can be calculated from the

Table III. Temperature–Time Combinations Used for Determination of Aging Curves

Alloy	Aging Temperature	Aging Time
206	463 K (190 °C)	0, 5, 15, and 30 min; 1, 2, 4, 8,
319	513 K (240 °C)	16, 32, 50, 64, and 100 h
356	483 K (210 °C)	
A356	433 K (160 °C)	
A356 + 0.5Cu	433 K (160 °C)	

relation, $\frac{x}{\sin\theta}$. The same thickness measurement method was applied to the other two alloys (206 and A356).

C. Aging Curve Determination

The evolution of strengthening precipitates during isothermal heat treatments and their effect on the mechanical response for the five cast alloys was determined through their respective aging curves. The solution-treated materials were sequentially aged for different times as per the aging temperatures given in Table III, and the hardness was measured after each of these time intervals. The time durations include both short-term (under-aging) and long-term (over-aging) heat treatments. Hardness measurement was carried out using a 10 mm spherical Brinell indentation at a load of 500 kg, and at least, four indentations were performed on each of the aged specimens.

D. Vickers Hardness Measurement

Mechanical characterization of the as-aged as well as pre-conditioned alloys were carried out using Vickers indentation at 5 kg load (HV5) on all the three faces (X, Y, and Z) at room temperature (Figure 1(b)). In addition, hardness was also measured on the Z-face in as-cast condition and after solution treatment. Indentation surfaces were metallographically polished up to 2500 grit SiC paper, and the indenter was kept in contact with the specimen surface for 10 seconds. A minimum of 10 indentations were performed to increase statistical reliability. The average hardness was calculated in SI units (GPa), and the error is expressed as the standard deviation of the dataset.

E. Thermophysical Property Measurement

Thermophysical properties of the as-aged as well as 573 K (300 °C) pre-conditioned alloys were measured using differential scanning calorimetry (DSC), laser flash diffusivity (LFTD), and dilatometry techniques. The specific heat capacity of the as-aged alloys was determined by DSC** using the three-run ratio method as

**Netzsch DSC 404C, Burlington, MA, USA

per ASTM E1269 from room temperature up to 773 K (500 °C). Disk-shaped specimens having diameter of 6 mm and thickness of 1 mm were heated and cooled in flowing argon at rates of 20 K/minute (20 °C/minute). A sapphire disk of the same dimensions was used as the reference standard. Platinum pans and lids were used for all runs.

The thermal diffusivity of the alloys was determined by LFTD† using the method described in ASTM E1461[67]

†Netzsch LFA 457, Burlington, MA, USA

from 298K to 723 K (25 °C to 450 °C) at an interval of

(a)

(b)

(c)
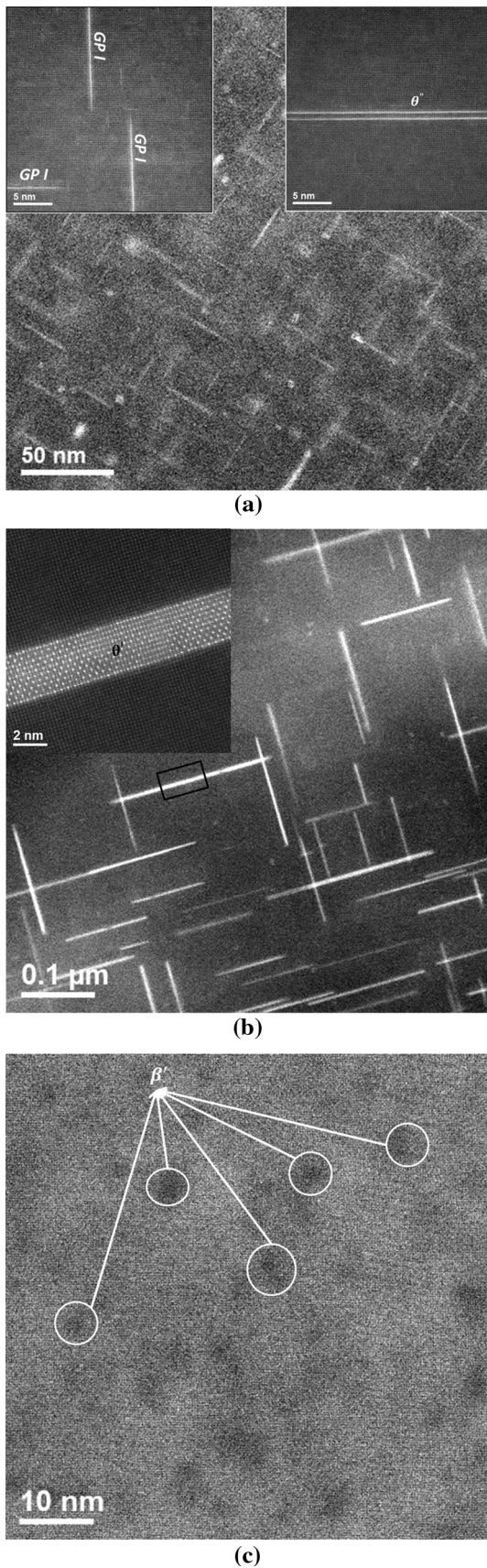
◄ Fig. 2—HAADF-STEM micrographs at lower magnification and insets: high magnification for (*a*) 206, (*b*) 319, and (*c*) A356. For (a) and (b), θ'' and θ' precipitates appear in bright and α-Al matrix in dark contrast at the low magnification. At high magnification (with near atomic resolution), the Cu atoms appear in bright and Al atoms in darker contrast. For (c), β' precipitates appear in darker contrast at low magnification. The zone axis is $\langle 001 \rangle_{Al}$ for all these micrographs.

25 K (25 °C). Measurements were also taken at 573 K (300 °C) and 373 K (100 °C) during cooling to investigate irreversible changes that might have occurred during heating. Disk-shaped specimens originally prepared from the longitudinal (parallel to *X*-direction as per Figure 1(b)) and transverse directions (parallel to *Y*-direction as per Figure 1(b)) of the cast blanks with diameter of 12.7 mm and thickness of 3 mm were used for this purpose. Tests were conducted in flowing argon, and both faces of the specimens were spray coated with colloidal graphite to increase emissivity of the surfaces. The dimensions and mass of the diffusivity specimens were used to calculate the room temperature density of the alloys.

Finally, the thermal expansion of the alloys was determined by horizontal dual push rod differential dilatometry‡ using the method described in

---

‡Theta Dilatronic IX, Port Washington, NY, USA

ASTM E228 from 293 K (20 °C) to 773 K (500 °C) at heating and cooling rates of 3K/minute (3 °C/minute). Measurements were taken on rod-shaped specimens cut from the longitudinal direction of the cast blanks having diameter of 4 mm and length of 25 mm. A sapphire reference standard of the same dimensions was used for all test runs. Tests were conducted in flowing helium. Each specimen was tested twice to investigate irreversible changes that might have occurred during heating.

III. RESULTS AND DISCUSSIONS

A. *Microstructure and Nano-structure of the As-aged Alloys*

Microstructure of the five cast alloys in as-aged condition is discussed in detail in Section III–A of Part I. The discussion included the description of key microstructural features in terms of size and morphology at various length scales using optical microscopy as well as SEM and EDS techniques. Similarly, Section III–B in Part I contain the details of various nano-scale precipitates that form in the as-aged alloys. To facilitate subsequent discussion on mechanical response and strength modeling, the STEM HAADF images from some of these alloys (206, 319, and A356) are presented in Figure 2.
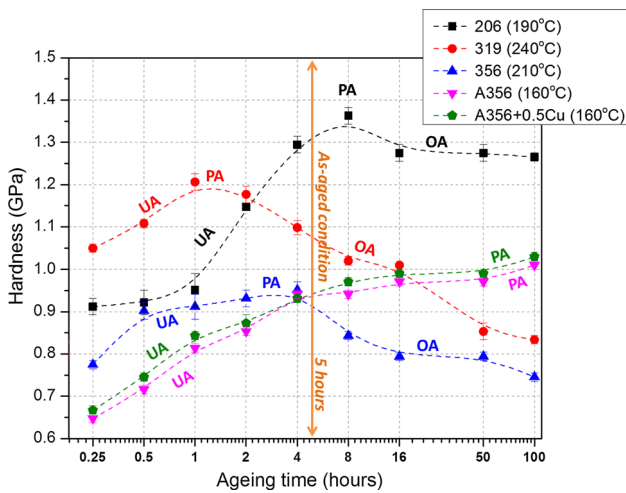
Fig. 3—Aging curve (Vickers hardness variation with respect to the heat treatment time) for the alloys determined from sequential indentation on solution-treated specimens. The heat treatment temperatures are mentioned alongside. Also the condition used for aging the solution-treated alloy blanks is indicated. *UA* under-aged, *PA* peak-aged, and *OA* over-aged.

B. *Mechanical Characterization*

1. *Aging curve determination*

The aging curves for Al-Cu (206), Al-Si-Cu (319), and one of the Al-Si (356) alloys display a common trend wherein the hardness continuously increases up to a peak value and decreases thereafter with heat treatment time (Figure 3). The two Al-Si alloys (A356 and A356 + 0.5Cu), on the other hand, initially display a hardness increase that later stabilizes and does not show any reduction with time. The nano-scale strengthening precipitates (θ'' and θ') in Al-Cu (206) and Al-Si-Cu (319) alloys are metastable compared to the equilibrium θ-Al$_2$Cu precipitate, while in case of the Al-Si alloys (356, A356 and A356 + 0.5Cu), the precipitates (β'' and β') are also metastable compared to the equilibrium β-Mg$_2$Si precipitate. The age hardening mechanisms for these alloys are influenced by the temperature (thermal activation) and time (kinetic barrier); an appropriate aging time and temperature combination is usually intended for optimal mechanical response by designing the size, number, morphology, and nature of the interfaces for the nano-scale metastable precipitates.[2,4,68–70] Dislocation–precipitate interaction in the aging conditions described in this manuscript is due to either (a) creation of new interfaces because of the shearing of coherent precipitate (GPI or θ'' and β'')[71] or (b) Orowan looping around semi-coherent precipitate (θ' and β').[30] Considerable strength increment is achieved once the precipitates are of appropriate size and spacing, sufficient in numbers, and with semi-coherent interfaces (for Orowan looping) so as to ensure adequate pinning points at optimal intervals.

For the Al-Cu precipitates in the 206 or 319 alloys, when the solution-treated alloy is aged, the Cu atoms initially form a single layer within the α-Al matrix (GPI-zones) and later transform to one unit cell thick θ'' precipitate; both of which are coherent with the α-Al

Fig. 4—Vickers hardness (HV5) measured on different surfaces (X-face, indentation direction||X; Y-face, indentation direction||Y and Z-face, indentation direction||Z) from cast billets of (*a*) 206, (*b*) 319, (*c*) 356, (*d*) A356, and (*e*) A356 + 0.5Cu pre-conditioned for 200 h at various temperatures. (*f*) Optical images of the micro-indents from specimens pre-conditioned at 523 K (250 °C), left: 206, middle: 319, and right: A356.

matrix so that they contribute only through interfacial strengthening at the beginning of aging; in this process, increase in the interfacial area occurs due to creation of new precipitate/α-Al matrix interface as matrix dislocations shear the precipitates.[22] This condition leads to a measurable hardness increase on aging and is typically referred to as the under-aged condition. With increasing time, hardness continuously increases once the precipitate transforms from coherent GPI and θ'' to semi-coherent θ' where the strength increments come through Orowan looping.[72] Peak hardness is generally obtained within the transition region between θ'' and θ' because of an optimal number density and precipitate spacing (peak-aged condition). Afterward, the semi-coherent interfaces of θ' precipitate provide a driving force for continued coarsening so that the hardness continuously decreases with heat treatment time as a result of loss in number density and increase in precipitate spacing (over-aged condition).[20,21,73,74] More about the precipitate coarsening effect on the strength decrease (relevant for over-aged conditions) is discussed in Section III–D.

The relative difference in the aging behavior of 206 and 319 with similar strengthening precipitates can be explained based on the thermodynamics and kinetics of aging sequence (GPI→ θ''→θ') with heat treatment. Comparing these two alloys, much higher initial hardness at equivalent time durations for the 319 alloy is related to the higher aging temperature by 50 K (50 °C) that accelerates the aging process (early transition of GPI and θ''→θ').[5] The additional thermal energy also ensures earlier attainment of peak-aging (1 hour) for 319 and rapid decrease in hardness afterward due to over-aging and related coarsening of θ' precipitates. For the 206 alloy, lower aging temperature not only produces a delayed transition of GPI and θ''→θ' transformation so as to achieve a longer peak-aging response (~8 hours) but also ensures slower hardness decrease due to coarsening of θ' on over-aging.

In the case of the Al-Si alloys, only the 356 alloy displays all three regimes of the aging curve (under-age, peak-age, and over-age), while the other two alloys (A356 and A356 + 0.5Cu) reach only the under and peak-aging regimes within the duration of the experiments. Peak-aging and subsequent over-aging in the latter two alloys are extremely sluggish as indicated by the stabilization of hardness after ~8 hours of aging. These Al-Si alloys with β-Mg$_2$Si strengthening precipitate show equivalent thermal response to θ-Al$_2$Cu precipitates (Coherent GPI → coherent β'' → semi-coherent β' → incoherent equilibrium β-Mg$_2$Si).[45,75,76] Relatively higher aging temperature for 356 (by 50 K, *i.e.*, 50 °C) as opposed to A356 or A356 + 0.5Cu ensures faster aging kinetics, much like the 319 alloy so that peak-aged and over-aged conditions are readily
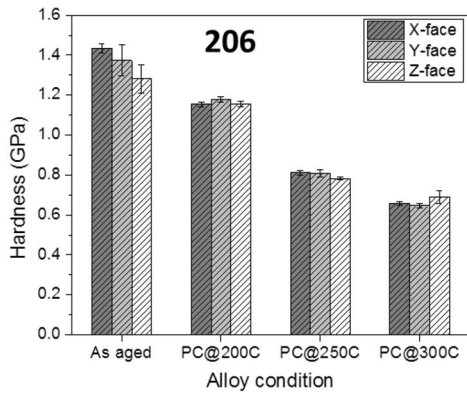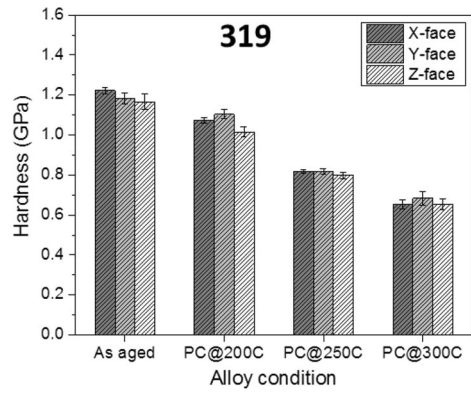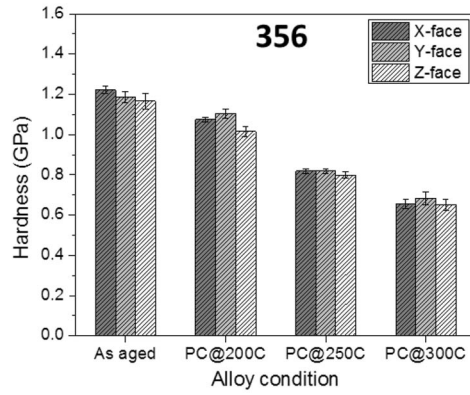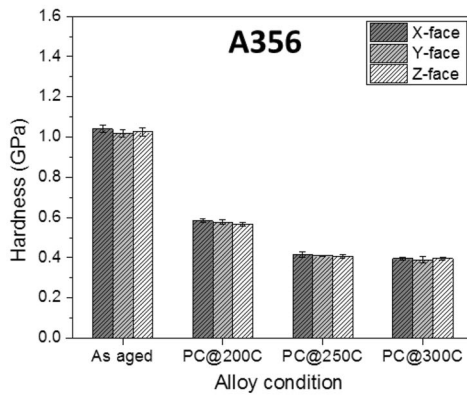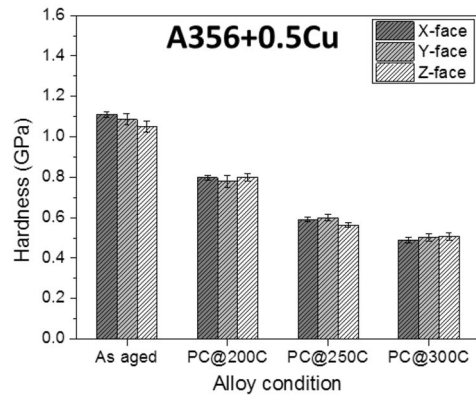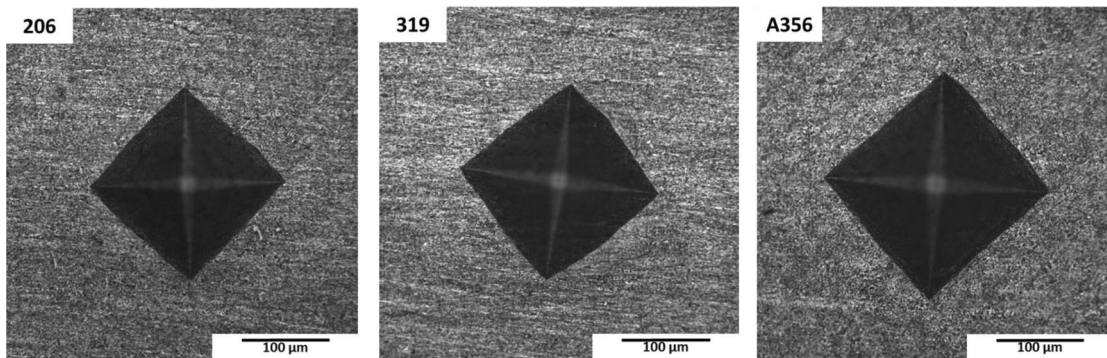
Table IV. Precipitates Dimensions, Corrections and Strength Increment Obtained from the Strength Modeling Considering $G = 25.4$ GPa, $b = 0.284$ nm and $v = 0.33$

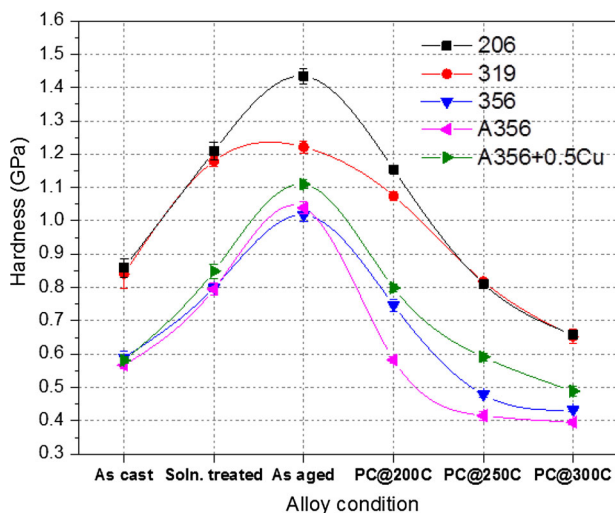| Alloy	Precipitate	Average Width (Measured), d_m (nm)	Average Thickness, t_t (nm)	Corrected (Actual) Width, d_t (nm)	Number Density, N_v (nm^{-2})	Volume Fraction, f	$\Delta\tau$ (MPa)	
206	GP-Zone	13.37	0.4	13.5	50.2×10^{-7}	0.0003	38.001	58.1
	θ''	22.66	1.42	23.1	24.6×10^{-7}	0.0015	13.15	
		32.41	2.5	33.2	7.5×10^{-7}	0.0016	6.35	
319	θ'	115.87	6.25	124.87	3.6×10^{-7}	0.0275	47.44	
A356	β'	7.06 (diameter, nm)		7.14	55.3×10^{-5}	0.079	54.55	

Fig. 5—Average Vickers hardness obtained at different conditions before and after the heat treatment (*PC* pre-conditioned). The alloys were pre-conditioned for 200 h.

achieved.[62–64,77] For the other two Al-Si alloys, an aging temperature of 433 K (160 °C) is not adequate to reach up to the semi-coherent β' stage within even 100 hours.

Based on the aging curves, it is concluded that for the heat treatment conditions employed in the present study, the alloy 206 is under-aged after 5 hours but not far from being in the peak-aged condition (T6), while the alloy 319 certainly exists in over-aged condition (T7). Furthermore, the alloy 356 is possibly peak-aged (T6) after 5 hours, while A356 and A356 + 0.5Cu alloys are in under-aged conditions.

2. Effect of heat treatment (solution treatment, aging, and pre-conditioning)

Vickers hardnesses measured from the three surfaces (X, Y, and Z, Figure 1(b)) are nearly identical for every individual alloy, after both the aging and pre-conditioning heat treatments (within the error limit) indicating isotropic mechanical response for all the alloys (Figures 4(a) through (e)). With increase in pre-conditioning temperature, the hardness drops on all three surfaces of the cast alloy blanks. The size of the Vickers indents in Figure 4(f) for various alloys (corner to corner distance ~200 to 250 μm) can be compared with the respective microstructural (grain size for 206 and SDAS or secondary dendrite size for 319, 356, A356,

and A356 + 0.5Cu, Table IV in Part I) and nano-structural (strengthening precipitates) features (Table IV); it is concluded that the hardness indeed represents the macroscopic mechanical response of the alloys. The invariance of hardness on different faces can be correlated to the homogeneous micro- and nano-structures that exist in the blanks after casting. The observation also provides the rationale to conduct indentation only from one face (Z-face) of the billets for aging curve determination in the previous section.

The effect of pre-conditioning heat treatment on the mechanical response of various alloys is evident from the results presented in Figure 5. Also, the hardness of respective alloys in as-cast and solution-treated conditions is included for comparison. The hardness for as-aged and pre-conditioned materials was averaged out from the three faces, while for the as-cast and solution-treated specimens, hardness was measured on the Z-face alone. The general trend is that the hardness is initially low after casting, then improves on solution treatment and reaches a maximum after aging. Long-term pre-conditioning decreases the hardness from the as-aged condition; reduction in hardness is drastic up to 523 K (250 °C) but becomes limited with increasing pre-conditioning temperature up to 573 K (300 °C) for all the alloys.

Considering that the strength of any of these alloys is primarily attributed to the nano-scale precipitates (and also contributed by other microstructural features but on a much lower scale than the former); the as-cast hardness is low since no strengthening precipitates have formed yet, and solid solution strengthening elements are segregated in the structure. Solution treatment increases as-cast hardness due to the solid solution strengthening effect from the major alloying elements (Cu in 206 and 319; Si and Mg in 356 & A356 and Si, Mg and Cu in A356 + 0.5Cu).[78] Aging at an optimized temperature–time combination finally leads to the appropriate size, number density, and spacing for strengthening precipitates that maximize the hardness.

Long-term pre-conditioning at lower temperature (473K, *i.e.*, 200 °C) significantly coarsens the strengthening precipitates and disrupts this optimized nano-structure, much in the same way as over-aging does, so much so that the precipitates eventually lose their strengthening contribution.[20,21,73,74] Again, the precipitate coarsening effect on the strength decrease is discussed in Section III–D. At sufficiently higher temperature [523 K (250 °C) or 573 K (300 °C)], coarsening

can largely remove the strengthening contributed by the nano-scale precipitates, and the final mechanical response is again controlled only by the microstructural features of the α-Al matrix; in this case, however, with a much lower contribution from solid solution strengthening elements which are captured within the coarsened strengthening precipitates. This makes the hardness value of the 523 K (250 °C) or 573 K (300 °C) pre-conditioned specimens even lower than that obtained for the corresponding hardness values in the solution-treated or as-cast condition. The adverse effect of pre-conditioning to the precipitate coarsening can be realized by comparing the SEM micrographs of pre-conditioned alloys in Figure 6 with the STEM HAADF micrographs of as-aged alloys in Figure 2. The nano-scale precipitates that formed after aging the three alloys (206, 319, and A356) have transformed and significantly coarsened after pre-conditioning at 573 K (300 °C) so much, so that these micron-sized precipitates can now be observed at much lower magnification. Increase in size is invariably associated with reduction in the number density and increase in spacing of the precipitates after pre-conditioning of the alloys.

Now comparing Al-Cu (206) and Al-Si-Cu (319), as-cast hardness for the two alloys is exactly equal when no nano-scale strengthening precipitates are present. Little difference occurs on solution treatment wherein higher hardness for 206 alloy can be attributed to the additional Cu in the composition (5 wt pct in 206 *vs* 3.17 wt pct in 319, Table I).[78] Significant hardness difference between 206 and 319 alloys in the as-aged condition is expected considering the alloy 206 is peak-aged (T6), while the alloy 319 is over-aged (T7) as per their respective aging curves (Figure 3).[72]
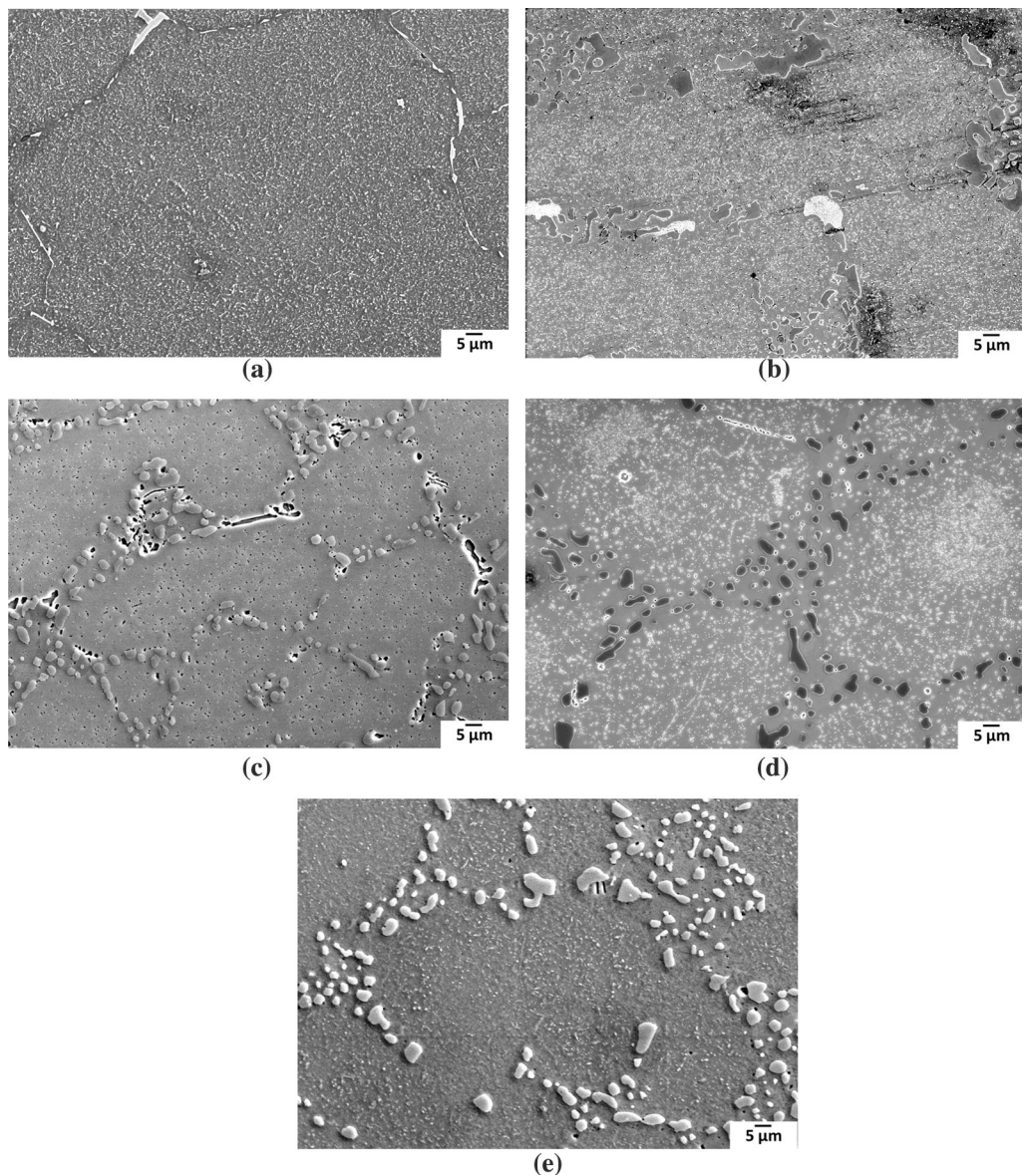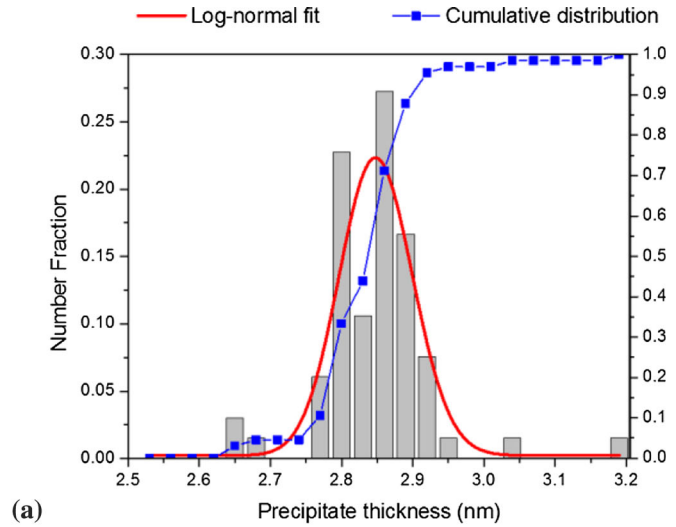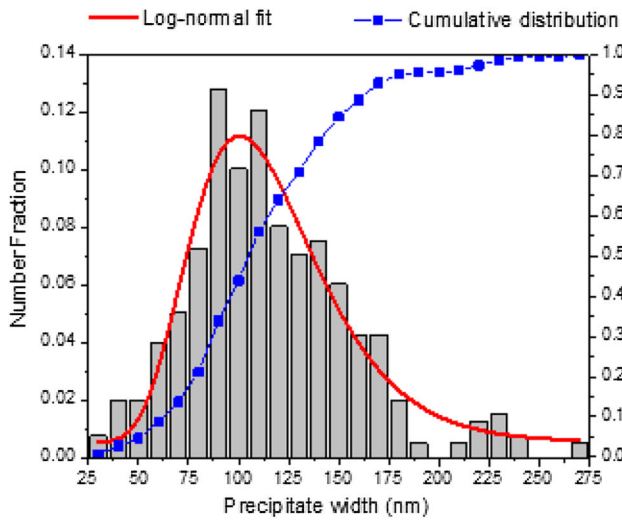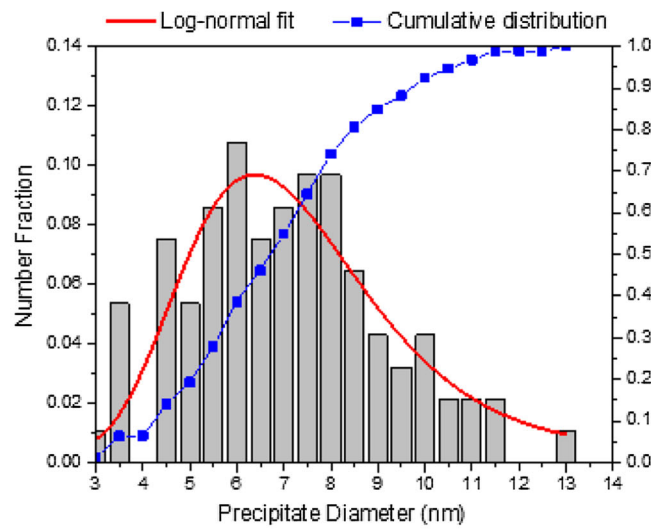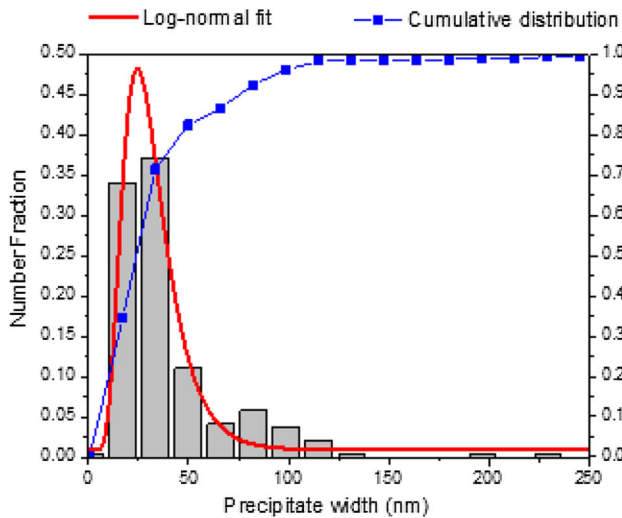

Fig. 6—SEM micrographs (SE mode) showing the microstructures of (*a*) 206, (*b*) 319, (*c*) 356, (*d*) A356, and (*e*) A356 + 0.5Cu after pre-conditioning for 200 h at 573 K (300 °C).
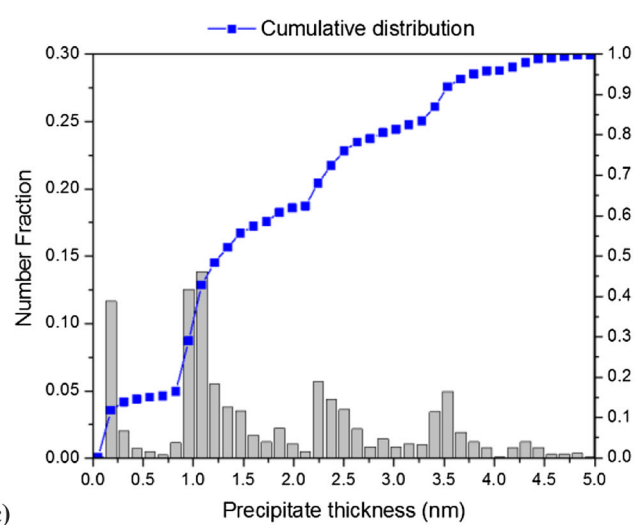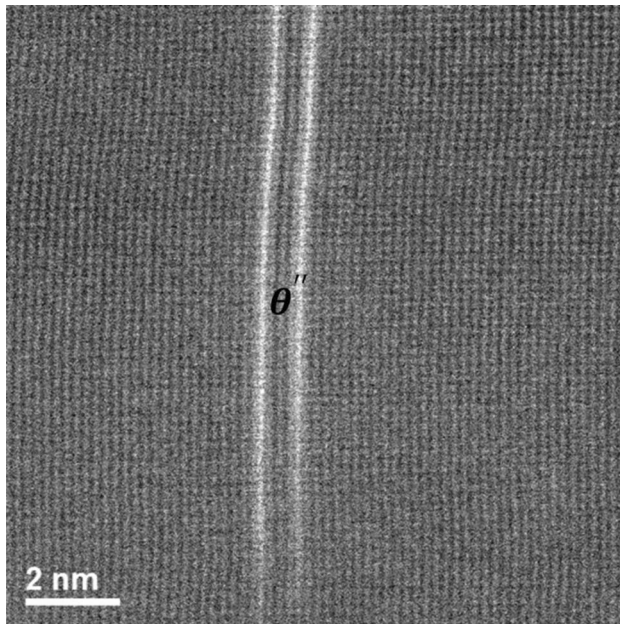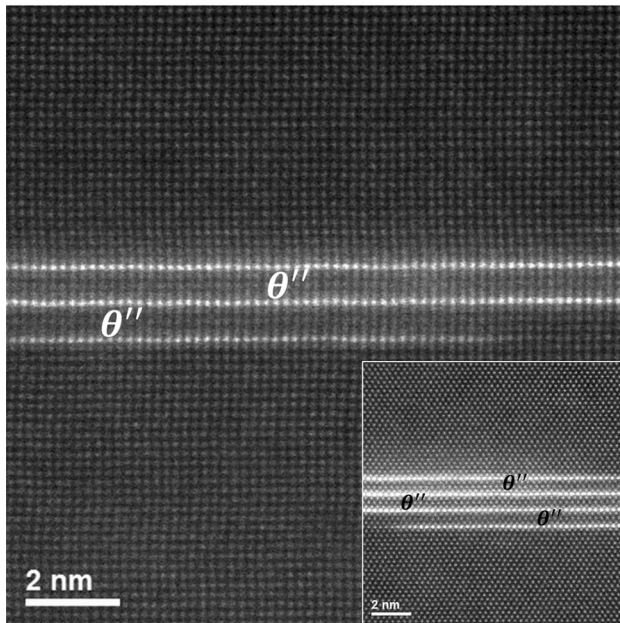
Fig. 7—Width (left) and thickness (right) distribution of the nano-scale strengthening precipitates (as measured from the image analysis of HAADF-STEM micrographs) for (*a*) 319 (θ') and (*c*) 206 (GPI and θ''); for A356 with β' only diameter distribution is shown in (*b*).

(a)

(b)

Fig. 8—HAADF-STEM micrographs for 206 alloy showing the state of θ'' precipitate, (a) as single unit cell with thickness ~1 nm and (b) as two and inset: multiple unit cell ensemble with thickness >2.5 nm. For (a) and (b), zone axis = $\langle 001 \rangle_{Al}$; for (b) inset, zone axis = $\langle 110 \rangle_{Al}$.

Hardness improvement on aging (relative to the solutionized condition) is in fact marginal for the 319 alloy (~3.5 pct) but significant for the 206 alloy (~18.5 pct). This observation is consistent with the STEM observations on these alloys in the as-aged condition; the alloy 206 contains GPI and θ'' precipitates with very fine size and spacing and high number density, whereas nano-structure for 319 is characterized by θ' precipitates with comparatively larger size and spacing and relatively
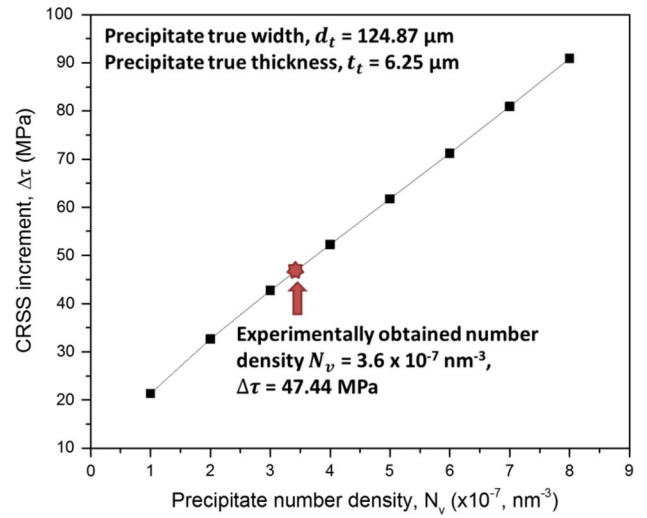
(a)
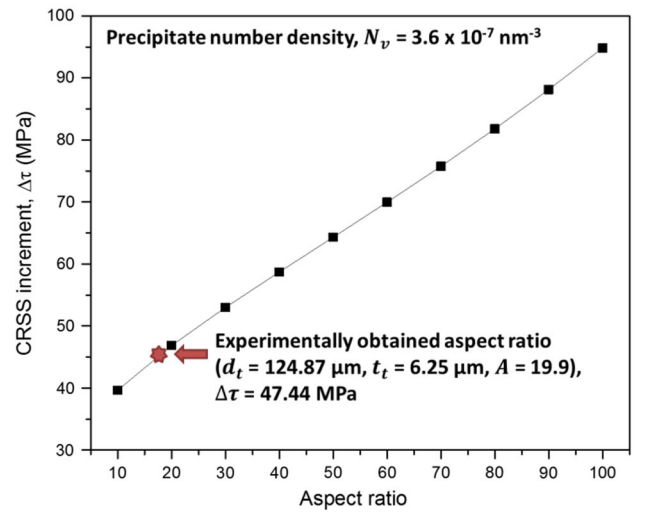
(b)

Fig. 9—Effect of change in (a) number density and (b) aspect ratio on the predicted CRSS increment as calculated for the 319 alloy (considering Orowan looping as per Eq. [3]) keeping all other parameters constant.

low number density (Figures 2(a) and (b)). The drop in hardness due to pre-conditioning at 473 K (200 °C) is lower for 319 (~12 pct) compared to that for 206 (~19.5 pct). Pre-conditioning at 473 K (200 °C) causes transformation of the GPI and θ'' precipitates to θ' and leads to rapid hardness drop for 206 alloy. The effect on alloy 319 is lesser since it is already over-aged at 513 K (240 °C) and contains coarse θ' precipitates. Further pre-conditioning at 523 K (250 °C, ~29 pct drop in hardness for 206 and 24 pct for 319 compared to 473K, *i.e.*, 200 °C values) and 573 K (300 °C, ~20 pct drop in hardness for both 206 and 319 compared to 523K, *i.e.*, 250 °C values) leads to an equivalent decrease in hardness for both these alloys.

The three Al-Si alloys (356, A356, and A356 + 0.5Cu) possess nearly equivalent hardness values in the as-cast condition (~0.55 GPa). After solution treatment, the hardness is exactly comparable for 356 and A356 (~0.8

Table V. Specific Heat Capacity, Thermal Diffusivity, and Thermal Conductivity of As-aged Alloys

T, K (°C)	Specific Heat Capacity (J/g °C)					Thermal Diffusivity (mm²/s)					Thermal Conductivity (W/m K)				
	356	A356	A356+0.5Cu	319	206	356	A356	A356+0.5Cu	319	206	356	A356	A356+0.5Cu	319	206
298 (25)	0.90	0.90	0.89	0.86	0.89	65.8	68.2	64.9	59.4	61.6	159	163	155	141	151
323 (50)	0.92	0.92	0.91	0.88	0.91	66.2	68.3	65.7	59.6	62.4	162	168	160	145	156
348 (75)	0.93	0.94	0.93	0.90	0.92	66.2	68.4	66.0	59.9	63.3	165	171	163	149	161
373 (100)	0.95	0.95	0.94	0.91	0.94	66.4	68.6	66.2	60.0	63.9	168	175	166	151	165
398 (125)	0.96	0.96	0.95	0.92	0.95	66.4	68.6	66.2	60.1	64.5	170	177	168	153	169
423 (150)	0.97	0.97	0.96	0.93	0.96	66.3	68.7	66.3	60.2	64.9	172	179	169	155	171
448 (175)	0.97	0.98	0.96	0.94	0.96	66.3	68.7	66.3	60.2	65.3	172	181	171	156	174
473 (200)	0.98	0.99	0.98	0.94	0.97	66.2	68.8	66.5	60.1	65.5	173	184	174	157	176
498 (225)	0.98	1.00	1.00	0.95	0.98	66.0	69.0	66.9	60.1	66.1	174	184	178	158	179
523 (250)	1.00	1.02	1.01	0.97	0.98	66.0	70.1	67.6	60.1	67.0	176	190	183	160	182
548 (275)	1.01	1.04	1.03	0.99	0.99	66.2	70.9	68.1	60.4	67.5	179	195	188	164	184
573 (300)	1.03	1.05	1.05	1.00	1.00	66.5	71.2	68.6	61.0	68.3	183	199	192	169	189
598 (325)	1.04	1.07	1.07	1.02	1.02	66.4	71.1	68.6	60.9	69.1	185	201	195	171	194
623 (350)	1.05	1.08	1.08	1.04	1.04	66.0	70.6	67.8	60.5	69.2	186	203	196	173	198
648 (375)	1.07	1.10	1.10	1.06	1.05	65.3	69.6	67.3	59.6	68.7	187	203	198	173	200
673 (400)	1.08	1.11	1.12	1.07	1.07	64.4	68.5	66.4	58.5	67.7	187	202	198	173	201
698 (425)	1.10	1.13	1.14	1.09	1.09	63.4	67.1	65.3	57.2	66.6	187	201	198	172	200
723 (450)	1.12	1.16	1.15	1.11	1.11	62.2	65.5	63.9	55.5	65.6	187	203	196	170	200

Density* @ 25 K (25 °C) (g/cm³)

356	A356	A356+Cu	319	206
2.68	2.66	2.68	2.76	2.76

*Density calculated from mass and dimensions of diffusivity specimens.

GPa) because of their similar composition but slightly higher for A356+0.5Cu (~0.85 GPa) due to the presence of additional Cu (0.44 wt pct) contributing to solid solution strengthening.[78] The hardness also differs after aging; A356+0.5Cu (~1.1 GPa) has a higher hardness compared to the other two alloys (~1.0 GPa). This difference is expected as A356+0.5Cu is nearly peak-aged, while 356 is over-aged as per the aging curves shown in Figure 3. Compared to the other two Al-Si alloys, for A356+0.5Cu, the drop in hardness is gradual on pre-conditioning and indicates increased thermal stability of the strengthening precipitates (β'). This is attributed to the additional Cu in the composition; Cu is known to enhance the stability of needle-shaped β' phase on aging when added in appropriate concentrations (~0.4 wt pct).[75] Cu also delays the coarsening of Q'-phase by segregating at the Q'/α-Al interfaces and helps maintain a fine dispersion of disordered L'-phase .

C. Strength Modeling

The hardness for the Al-Cu alloy (206) in the as-aged condition is higher than the Al-Si-Cu alloy (319) containing similar Al-Cu nano-scale precipitates (GPI and θ'' vs θ'); the difference being as significant as ~17 pct. Also, the strength of the Al-Si alloys (e.g., A356) is less (~17.5 pct) than that of the Al-Si-Cu alloy (319) even though both of them are characterized by coarse and over-aged strengthening precipitates (θ' vs β'). These differences can be better explained by implementing a strength model that was developed on the basis of size, number density, and aspect ratio of the nano-scale strengthening precipitates.[2] In the present context, strength modeling is carried for as-aged 206 (GPI and θ''), 319 (θ'), and A356 (β') alloys in accordance with the STEM observations and corresponding image analysis. Previous observations suggest that Orowan looping is the only precipitate–dislocation interaction mechanism for semi-coherent and shear resistant strengthening precipitates like θ' in 319 or β' in A356 alloys.[22,30,64,79–81]

The basic governing equation for strength increment via Orowan mechanism in case of plate-shaped θ' precipitate is given by the following[22]:

$$\Delta\tau = \left\{ \frac{Gb}{2\pi\sqrt{1-v}} \right\} \left\{ \frac{1}{0.931\sqrt{\frac{0.306\pi d_t t_t}{f}} - \frac{\pi d_t}{8} - 1.061 t_t} \right\} \times \left\{ \ln \frac{1.225 d_t}{b} \right\}$$

[1]

and that for the rod-shaped β' precipitates, it is given as:

$$\Delta\tau = \left\{ \frac{Gb}{2\pi\sqrt{1-v}} \right\} \left\{ \frac{1}{\left(\frac{1.075 x 1.1663}{\sqrt{f}} - 1.316 \right) r} \right\} \left\{ \ln \frac{1.316 r}{b} \right\}$$

[2]

where $\Delta\tau$ is the increment in critical resolved shear stress (CRSS); d_t and t_t are the effective width and thickness of plate-shaped θ' precipitate, respectively; r is the effective diameter of rod-shaped β' precipitates; and f is the volume fraction of precipitates. The values for G, shear modulus of α-Al matrix = 25.4 GPa; $\vec{b}$, burgers vector for $\frac{1}{2}\langle 110\rangle_{Al}$ dislocations on $\{111\}_{Al}$ slip plane = 0.284 nm and ν, Poison's ratio = 0.33 for FCC metals are obtained from References 82 through 84. Two important assumptions are made about the θ' precipitates while developing Eq. [1], (a) they grow with a habit plane parallel to $\{001\}_{Al}$ and (b) they are arranged on a triangular array in the $\{111\}_{Al}$ slip plane.[22] The assumption for the β'-precipitates is that $\langle 100\rangle_{Al}$ is the preferred growth direction with circular cross section so that only the diameter (r) is considered important in Eq. [2].[22] In case of the θ' precipitates, an improvement to Eq. [1] can be made by assuming a random distribution of plate-shaped θ' precipitates. The modified equation as per Reference 79 considering $f = \frac{N_v \pi d_t^2 t_t}{A_s d_t}$, where N_v is the number density of the precipitates, and A_s is the total area in the STEM micrograph:

$$\Delta\tau = \left\{\frac{Gb}{2\pi\sqrt{1-\nu}}\right\}\left\{\frac{1}{\frac{1.23\times 1.03}{\sqrt{N_v}d_t} - \frac{\pi d_t}{8} - 1.061 t_t}\right\}\left\{\ln\frac{0.981\sqrt{d_t t_t}}{b}\right\}$$

[3]

For the coherent GPI or θ'' precipitates in 206, strength increment occurs through the creation of newer interfaces due to dislocation–precipitate interaction and not by Orowan looping.[71] The effective relation that describes such interfacial strengthening for these shearable plate-shaped precipitates is given by[22]:

$$\Delta\tau = \left(\frac{0.908 d_t}{t_t^2}\right)\left(\frac{bf}{\Gamma}\right)^{\frac{1}{2}}\gamma_i^{\frac{3}{2}}$$

[4]

where d_t and t_t are the effective width and thickness of GPI or θ'' precipitates, respectively; γ_i is the interfacial energy and dislocation line tension, Γ is expressed as: $\Gamma = \frac{Gb^2}{2\pi}\ln\sqrt{\frac{d_t^2}{2b^2 f}}$; γ_i for GPI or θ'' precipitates can be considered equivalent to the interfacial energy of the coherent interfaces of θ' precipitates ($\gamma_i = 0.21$ J/m^2) since the θ' precipitates actually forms out of the coherent interfaces (broad faces) of θ'' precipitates.[14,43] An additional issue for the 206 alloy is to develop the summation law for overall strength increment ($\Delta\tau$) from the individual contribution due to GPI or θ'' precipitates [($\Delta\tau)_{GPI}$ and ($\Delta\tau_{\theta''}$)], given by[85]

$$(\Delta\tau)^q = \left\{(\Delta\tau)_{GPI}\right\}^q + \left\{(\Delta\tau)_{\theta''}\right\}^q$$

[5]

where the exponent q defines the order of superposition of various strengthening contributions in the addition law and usually varies between 1 (no overlapping) to 2 (complete overlapping).[86] It is further important to consider several stereological issues ONLY for GPI, θ'' and θ' precipitates while calculating the microstructural

input parameters (width, thickness, and number density) because of their plate-shaped morphology and preferred habit plane and growth direction. These input parameters are measured experimentally from image analysis of the STEM micrographs as explained in Section II–B.

The measured mean width of the precipitate d_m (average linear intercept), is to be corrected for the finite thickness of the TEM foil in the direction of the beam.[23,79] The importance of this correction is realized because of the fact that the thin foil actually causes a projection of the precipitates contained within the 3D observation volume. This may cause a truncation problem in size measurement of the precipitates since they are characterized with a large aspect ratio. The average width/diameter for the precipitates (GPI, θ'', θ', and β') in that case are often comparable to the foil thickness and truncation occurs at the upper or lower foil surface. The foil thickness along the $\langle 001\rangle_{\alpha\text{-Al}}$ zone axis was measured to be 247 nm for 319, 260 nm for 206, and 129 nm for A356 alloys following the methods described in Section II–B (Figure 1(b)).

Assuming a disk shape in 3D for simplicity, which is a reasonable assumption at least for θ'' and θ', the true diameter, d_t is related to the mean diameter d_m by the relation: $d_m = \left(\frac{t + \frac{\pi}{4}d_t}{t + d_t}\right)d_t$ where $\frac{\pi d_t}{4}$ is the mean planar diameter of the precipitate plates and t is the foil thickness in the beam direction. Solving the quadratic equation provides the following:

$$d_t = \frac{2(d_m - t) \pm 2\sqrt{(d_m - t)^2 + \pi d_m t}}{\pi}$$

[6]

Two additional issues need to be considered for the accurate calculation of the microstructural input parameters for GPI, θ'' and θ' precipitates: (a) measurement of precipitate thickness and (b) calculation of precipitate number density. The thickness measurement is difficult from low-magnification STEM images since most of the precipitates are hardly a few pixels thick, and this introduces a large scatter in the measured dataset. Again, use of low-magnification STEM images is unavoidable due to the statistical reliability of the size measurement in the first place. This imposes a challenge for actual strength prediction, as the error associated with an incorrect precipitate thickness measurement is usually large. A corrective measure suggested in Reference 30 is to determine a correction factor by comparing the thickness measurement for the same precipitate from high-magnification STEM images (Figure 2(a) inset) to that from low-magnification STEM images (Figure 2(a)). This correction factor is then to be used for accurate and statistically significant thickness measurement from low-magnification STEM micrographs. The correction factor is calculated to be ~0.5 for 206 and 319 alloys.

The next issue is to calculate the number density of GPI, θ'' and θ' precipitates with $\{001\}_{Al}$ habit plane. As has been explained in Section III–C of Part I, only two variants are usually observed with adequate contrast in the STEM images with $\langle 001\rangle_{Al}$ zone axis. This third invisible variant should nonetheless occupy a different

fraction of the unit microstructural area compared to the other two visible variants on the $\{001\}_{Al}$ planes under observation. Thus, the effective number of precipitates within any given microstructural area is not equal to simply three times the number of any one kind of variant. If the number of the two visible precipitate variants (N_1 and N_2) is known, then the number of precipitate in the third (unseen) dimension can be estimated as [23,79]

$$N_3 = \left(\frac{N_1 + N_2}{2}\right)\left(\frac{t + d_t}{\sqrt{A_S}}\right) \qquad [7]$$

where A_s is the total area in the STEM micrograph. The total number of precipitates then becomes:

$$N_T = \left(\frac{N_1 + N_2}{2}\right)\left(1 + \frac{t + d_t}{2\sqrt{A_S}}\right) \qquad [8]$$

and the number density,

$$N_v = \frac{N_T}{A_S(t + d_t)}. \qquad [9]$$

In case of the alloy A356, because of the assumption of circular cross section for rod-shaped β' precipitates with $\langle 100 \rangle_{Al}$ growth direction, NO stereological correction is required from STEM micrographs with $\langle 001 \rangle_{Al}$ zone axis, neither for the measured diameter nor for the number density or volume fraction.[87] The measured precipitate diameter is, however, corrected for the finite TEM foil thickness (129 nm).

Table IV summarizes the size, number density, and volume fraction of the strengthening precipitates in the three alloys considered (206, 319, and A356). These measurements are based on the weighted average of the distributions of the linear intercepts (number fraction *vs* corresponding dimension) from the image analysis of the STEM micrographs (Figure 7). In case of the alloy 319 with θ' precipitates, both the width and thickness distributions are unimodal and can be fitted with log-normal functions with adequate reliability (Figure 7(a)). The calculation of weighted average is also straightforward and represents unique values for width and thickness. Similarly, the alloy A356 with β' precipitates represents unimodal log-normal distribution of precipitate diameters that can be used for average diameter calculation without ambiguity (Figure 7(b)).

The alloy 206 represents unimodal log-normal width distribution for the strengthening precipitates but the thickness distribution is certainly multimodal (Figure 7(c)). Important to note that this alloy contains two different forms of the strengthening precipitate (GPI with single Cu layer and θ''). A careful comparison of the STEM micrographs with the thickness distribution suggests that the GPI precipitates are usually <1 nm in thickness, whereas θ'' forms with various thickness (either 1 to 2.25 nm or >2.5 nm). Here lies an apparent discrepancy as per the structural identity of θ'' precipitates are concerned. Theoretically, being one unit cell thick and containing three atomic layers of Al and two layers of Cu in $\langle 001 \rangle$ direction (as also evident from

Figure 8(a)), the thickness of θ'' should be <1 nm (~0.79 nm as per Reference 43). In that context, measured θ'' thickness of ~1 to 2 nm seems justified considering the error involved in image analysis; however, θ'' thickness >2.5 nm is certainly an overestimation and likely to be a misinterpretation of the measured dataset. A careful scrutiny of the STEM micrographs again revealed that such θ'' precipitates of thickness >2.5 nm are, in most occasions, an ensemble of multiple θ'' precipitates (Figure 8(b)). From the strength modeling point, it seems rational to consider such ensemble of θ'' precipitates being a separate entity with specific size and number density that also participate in strength increment *via* interfacial strengthening. The measured dataset for 206 alloy is therefore divided between GPI and θ'' (comprising of single and multiple unit cells) as per this size ranges and the corresponding average width, thickness, number density, and volume fraction was calculated separately (Table IV).

Table IV summarizes the CRSS increment for these alloys using Eqs. [1] to [4]. For the alloy 206, a linear summation ($q = 1$) is used in Eq. [5] assuming that the contribution from GPI and θ'' do not overlap. This assumption seems reasonable considering that both types of precipitates contribute through only interfacial strengthening.[86] The increase in CRSS due to various precipitates in these alloys thus varies in the order $(\Delta\tau)_{206} > (\Delta\tau)_{A356} > (\Delta\tau)_{319}$ (Table IV). This calculated order of CRSS increment somewhat deviates from the experimentally obtained hardness variation between these three alloys in as-aged condition, *i.e.*, $(H_v)_{206} > (H_v)_{319} > (H_v)_{A356}$ (Figure 5). It is important to note that several microstructural factors (*e.g.*, solid solution strengthening, coarse intermetallics, grain size or SDAS, *etc.*) other than the nano-scale precipitates contribute to the overall mechanical response of these alloy systems.[30] This is why a one-to-one comparison of CRSS increment and Vickers's hardness is not attempted here.

Between the alloys 206 and 319 with similar Al-Cu-type strengthening precipitates, the CRSS increment is higher for the former alloy (206 with interfacial strengthening, $\Delta\tau = 58.12$ MPa) compared to the later alloy (319 with Orowan looping $\Delta\tau = 47.44$ MPa). Also, out of the two different forms of the precipitates, GPI causes much higher contribution (($\Delta\tau)_{GPI} = 38.4$ MPa) to the CRSS increment than the θ'' phase (($\Delta\tau)_{\theta''} = 19.73$ MPa) in 206 alloy. The primary reasoning for such high level of strengthening achieved from much finer GPI precipitates is their high number density that increases effective pinning points for the dislocations.

It is also interesting that although the number density of the θ' precipitates in 319 alloy (3.6×10^{-7} nm^{-2}) is an order of magnitude smaller than the θ'' precipitates in 206 alloy (32.42×10^{-7} nm^{-2}), the former precipitates still render much higher increment in CRSS compared to that from the later. This is simply because, as also appears from Eqs. [1] to [4], the CRSS increment is a synergistic effect of width, thickness, and number density of the strengthening precipitates that collectively decides the extent of Orowan looping (319 or A356) or

interfacial strengthening (206).[2] Individual θ'' precipitates are less effective for dislocation–precipitate interaction *via* interfacial strengthening because of their smaller width and thickness even when the occurrence of such interactions is more probable for this precipitate. Then again, CRSS increment for the alloy A356 with β' precipitates is higher ($\Delta\tau = 53.75$ MPa) than that of the alloy 319 with θ' precipitates even though the former precipitates are much finer than the later and both of them obtain strength increments by an Orowan looping mechanism. The difference again lies in the number density; β' precipitates with nearly four orders of magnitude higher number density on the slip plane than the θ' precipitates can have a significant influence on the dislocation motion.

D. *Effect of Precipitate Coarsening on the Mechanical Behavior*

The effect of coarsening of the nano-scale precipitates on the mechanical properties of the three alloys (206, 319, and A356) can be best realized during the aging (over-aged condition, Figure 3) or pre-conditioning (Figure 5) heat treatments. In either case, precipitate coarsening occurs on prolonged heat treatment and results in a significant decrease in room temperature hardness. To explain this further on the basis of the strength models, one needs to check the parameters in Eq. [3] (Orowan looping for 319 with), Eq. [2] (Orowan looping for A356 with β'), or Eq. [4] (interfacial strengthening for 206 with θ'' or GPI) that are to be affected by precipitate coarsening. Also important to consider is how such changes in precipitate parameters ultimately affects the CRSS increment ($\Delta\tau$) for these alloys.

The coarsening on heat treatment (over-aging or pre-conditioning) causes: (i) a decrease in the number density of the precipitates (N_v) and (ii) an increase in the width, d_t; thickness, t_t (for θ', θ'' or GPI); or radius, r (for β') of these precipitates in Eqs. [1] to [4]. Due to the second factor, effectively, the aspect ratio of the disk-shaped θ', θ'', or GPI precipitates decreases on

Fig. 10—Specific heat capacity, C_p, as a function of temperature for a representative Al-Si (356) alloy in as-aged condition during heating and cooling. The dotted black line and corresponding black arrows indicate the linear interpolation to estimate steady state, C_p values for calculation of thermal conductivity.

coarsening.[79] It is important to note that these parameters (N_v, d_t and t_t or r) are interrelated in the sense that it is not possible to alter any one of them independent of the others. For example, any increase in size (width, thickness or radius) or reduction in aspect ratio will invariably cause a reduction in the number density and vice-versa.[30] Both the decrease of N_v, being in the numerator, or increase of d_t, t_t or r in the denominator (in Eqs. [2] to [4]) will result in the reduction of $\Delta\tau$. Phenomenologically, this means that the pinning points are farther apart and the dislocation–precipitate interactions are diminished as a result of coarsening. Overall, the strength increment from the precipitates is less effective, and the alloy strength decreases on over-aging or pre-conditioning.

To further elucidate the effect of the precipitate coarsening on the strength properties, Figure 9(a) shows the predicted change in $\Delta\tau$ with the number density of the θ' precipitates in case of 319 alloy. The calculations are made by assuming the rest of the precipitate parameters remain constant in Eq. [3]. $\Delta\tau$ decreases monotonically with the reduction in number density and reduced to almost half when the number density comes down to half of the initial value. The effect of change in precipitate size can be better understood if the CRSS increment in Eq. [3] is expressed in terms of the aspect ratio rather than individually considering precipitate width and thickness. Assuming that θ' precipitates are thin circular disk,[79] the CRSS increment can be written in a modified form as

$$\Delta\tau = \left\{\frac{Gb}{2w\sqrt{1-v}}\right\}\left\{\frac{1}{1.21\left(\frac{1}{fAN_v^2}\right)^{\frac{1}{6}}-0.424\left(\frac{fA}{N_v}\right)^{\frac{1}{3}}-1.146\left(\frac{f}{N_vA^2}\right)^{\frac{1}{3}}}\right\}$$
$$\times\left\{\ln\left[\frac{1.063}{b}\left(\frac{f}{N_v\sqrt{A}}\right)^{\frac{1}{3}}\right]\right\}$$

[10]

where $A = \frac{d_t}{t_t}$; $t_t = \left(\frac{4f}{\pi N_v A^2}\right)^{\frac{1}{3}}$; and $d_t = At_t = \left(\frac{4fA}{\pi N_v}\right)^{\frac{1}{3}}$. Figure 9(b) then suggests that when the aspect ratio of the θ' precipitates decreases, the calculated strength increment ($\Delta\tau$) also decreases for the same number density. Figures 9(a) and (b) indicate that the reduction in $\Delta\tau$ with aspect ratio is smaller compared to the corresponding reduction of CRSS with number density. In summary, it is stated that the hardness reduction due to over-aging or pre-conditioning is a superimposition of the two effects considered namely, reduction in number density and aspect ratio of the strengthening precipitates.

E. *Thermophysical Property Characterization*

The specific heat capacity curves measured from the DSC analysis for the candidate Al-Cu (206), Al-Si-Cu (319), and Al-Si (356) alloys in as-aged condition display both endothermic and exothermic peaks. For simplicity, only the relevant curve for 356 alloy is shown in Figure 10. These peaks are possibly caused by the enthalpy associated with coarsening or dissolution
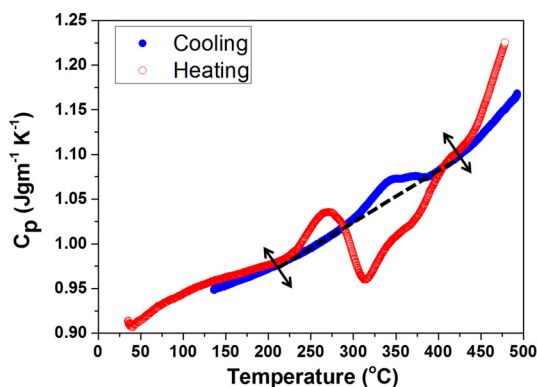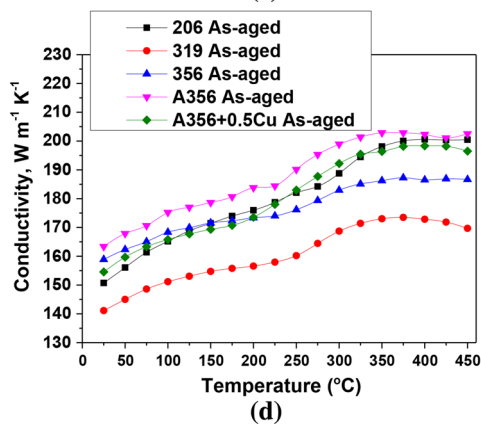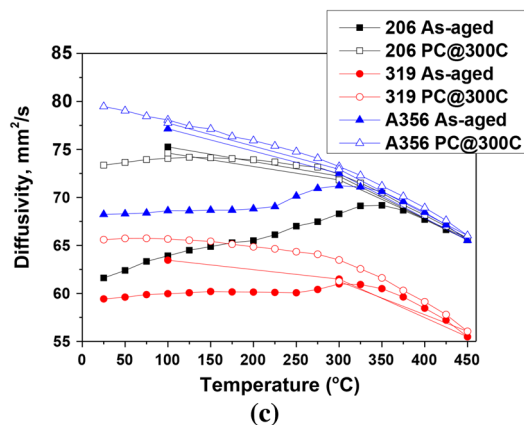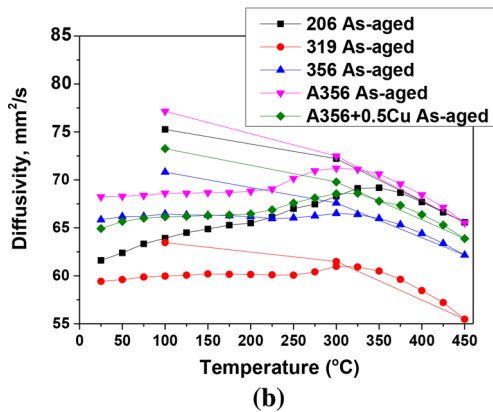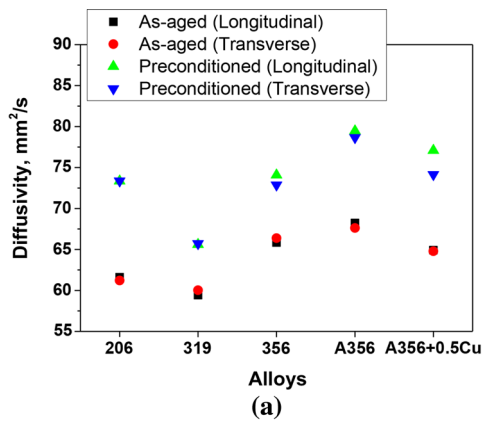
(a)

(b)

(c)

(d)

◀ Fig. 11—(*a*) Room temperature thermal diffusivity of the cast alloys in the longitudinal and transverse directions for as-aged condition and after the 573 K (300 °C) pre-conditioning; (*b*) variation in thermal diffusivity of the as-aged alloys as a function of temperature (results during cooling at 573K, *i.e.*, 300 °C and 373K, *i.e.*, 100 °C are also shown); (*c*) comparison of variation in thermal diffusivity with temperature for three representative alloys (206, 319, and A356) in as-aged condition and after the 573K, *i.e.*, 300 °C pre-conditioning; (*d*) variation in the thermal conductivity of the as-aged alloys as a function of temperature.

reactions occurring in this temperature range.[88] The steady state specific heat capacity, C_p, for these alloys is determined from the linear interpolation of the corresponding DSC curves through the region of precipitate reactions (indicated in Figure 10). These C_p values are summarized in Table V.

Next, Figure 11(a) represents the thermal diffusivity at room temperature for the five alloys. No difference in diffusivity is noted for the two test directions, longitudinal and transverse, for any of alloys. This directional invariance supports complete homogeneity of microstructure for these alloys (discussed in Section III–A in Part I) as well as nano-structure (which is also reflected in their mechanical response from various planes of the alloy blanks, Figure 4) after casting, aging, or pre-conditioning. The Al-Si alloys (356, A356, and A356 + 0.5Cu) show slightly higher thermal diffusivity than either Al-Cu (206) or Al-Si-Cu (319) alloys in the as-aged condition (Figure 11(a)). This difference is surprising given that the number density of nano-scale precipitates in Al-Cu (GPI or θ'' in 206) or Al-Si-Cu (θ' in 319) alloys is much lower than the Al-Si (β' in A356) alloys (Table IV). This should in effect decrease the number density of phonon scattering centers for the two former alloys.[89] This discrepancy is possibly related to the plate-shaped morphology of the GPI, θ'' or θ' precipitates which are more effective in phonon scattering compared to the rod-shaped cylindrical precipitates in Al-Si alloys.[90–92] This may also happen due to the additional phonon scattering caused by the point defects from the mass difference between the aluminum matrix atoms and the copper solid solution atoms.[93] This additional aluminum/copper mass effect of phonon scattering is much larger than that for aluminum/silicon and, therefore, could also lower the thermal diffusivity of the Al-Cu and Al-Cu-Si alloys.[94]

The 573 K (300 °C) pre-conditioning has increased the diffusivity of all alloys although the changes are not appreciable for the alloy 319. This again supports the nano-scale precipitate (GPI or θ'' in 206, θ' in 319 and β' in A356)—phonon scattering correlation as described previously. Coarsening of these precipitates on pre-conditioning reduces the number density of the nano-scale precipitates so that the scattering centers also become fewer and the thermal diffusivity increases for all the alloys.[91] The nano-scale θ' precipitates in alloy 319 undergo lesser coarsening, relatively, on pre-conditioning since this alloy was already over-aged to T7

condition and, therefore, the thermal diffusivity of 319 alloy was the least affected as a result of pre-conditioning among all the alloys considered.

Figure 11(b) shows the thermal diffusivity variation as a function of temperature for all the alloys in as-aged condition (corresponding values are given in Table V). Only results for the longitudinal specimens are presented since no statistically significant difference was noted between the two specimen orientations. The Al-Si (356) and Al-Si-Cu (319) alloys show small increases in diffusivity with temperature up to the 498 K to 548 K (225 °C to 275 °C), rapid increase up to ~623 K (350 °C), and decrease afterward till the maximum temperature (723 K, i.e., 450 °C). The Al-Cu (206) alloy, however, has a different behavior; diffusivity initially increases at a faster rate than the rest of the alloys, goes through a maximum at ~623 K (350 °C), and decreases afterward.

This difference between the alloy systems is again possibly caused by the relative size and number density of the nano-scale precipitates.[88,94] Both 356 and 319 alloys exist in over-aged condition with relatively coarser β' or θ' precipitates. The temperature increase therefore affects the nano-structure to a lesser extent for them, and the number of scattering centers is also affected marginally on heating up to ~523 K (250 °C). Coarsening proceeds at a faster rate at temperatures ≥523 K (250 °C), and as a result, diffusivity undergoes a peak value for these two alloys. This variation in diffusivity with temperature for the two alloys (356 and 319) can be correlated with their hardness variation during pre-conditioning in Figure 5; a stiff drop in hardness occurs between 473 K (200 °C) and 523 K (250 °C) suggesting change in the nano-structure. The precipitates may dissolve at even higher temperatures (near the solvus) when diffusivity also begins to decrease due to the additional point defects from increasing Cu in solid solution with the Al matrix.[93]

For the alloy 206 which is under-aged at the beginning, similar changes in diffusivity occur with increasing temperature. This increase in diffusivity with temperature is, however, much higher and sharper unlike 319 or 356. The continued coarsening and/or phase transformation (GPI $\rightarrow \theta'' \rightarrow \theta' \rightarrow \theta$) of the nano-scale precipitates results in rapid loss in the number of scattering centers and a simultaneous increase in thermal diffusivity with increasing temperature. Higher diffusivity values are measured at 573 K (300 °C) and 373 K (100 °C) during cooling for all the as-aged alloys suggesting irreversible changes upon heating to 723 K (450 °C).

After 573 K (300 °C) pre-conditioning, the micro- and nano-structure of all the alloys stabilize, and no further change is expected on heating. This is also evident from Figure 5; not much drop in hardness occurs for the alloys between 523 K (250 °C) and 573 K (300 °C) pre-conditioning. For pre-conditioned alloys (206, 319, and A356 alloy for example, Figure 11(c)), the thermal diffusivity variations with temperature are similar during heating and cooling for any single alloy. The thermal diffusivity variation for the pre-conditioned alloys, in fact, nearly overlaps with the corresponding curves for the as-aged alloys measured during cooling.

The combined effect of specific heat and thermal diffusivity variation with temperature is realized from the thermal conductivity variation of the as-aged alloys, which is expressed as

$$\kappa = \alpha C_p \rho \qquad [11]$$

where C_p is the specific heat capacity; α is the thermal diffusivity; ρ is the density of the alloys; and κ is the thermal conductivity. Thermal conductivity is important for cylinder heads since it determines (a) heat transfer during casting and service for these complex shapes and (b) dimensional stability of the finished parts throughout the heat treatment schedule.[95] The variation in thermal conductivity of the as-aged alloys as a function of temperature is presented in Figure 11(d). Diffusivity and density values were not corrected for dimensional changes caused by thermal expansion. These effects of thermal expansion on diffusivity and density partially cancel out, and the resulting error in thermal conductivity is small with respect to the overall uncertainty of the measurement (~7 pct).

The Al-Si-Cu alloy (319) exhibits the lowest and A356 the highest thermal conductivity over the entire temperature range. The thermal conductivity of the alloy 206 varies in a manner nearly identical to the alloy A356 + 0.5Cu at all temperatures. The alloy 356 initially shows the same variation as 206 or A356 + 0.5Cu but deviates to a reduced thermal conductivity after ~473 K (200 °C). This is expected since both specific heat and thermal diffusivity vary in the same order, i.e., $(C_p)_{319} < (C_p)_{206} < (C_p)_{A356/356/A356+0.5Cu}$ and $(\alpha)_{319} < (\alpha)_{206} < (\alpha)_{A356/356/A356+0.5Cu}$ for lower part of the temperature range (Table V). Also, $(C_p)_{206} \approx (C_p)_{356/A356+0.5Cu}$ and $(\alpha)_{206} \approx (\alpha)_{356/A356+0.5Cu}$ so that thermal conductivity of these three alloys (206, 356, and A356 + 0.5Cu) are nearly same in the higher temperature range.

F. Implications for Cylinder Heads

The alloys described here are candidates for cylinder head application in automobile engines. The cylinder head is among the most thermally sensitive components of an engine. Temperature rise can lead to crack formation if strength is below the developed thermal stresses. An effective way to manage thermal stresses is to efficiently dissipate heat through higher thermal conductivity alloys. As discussed, mechanical strength and thermal conductivity display opposing trends toward coarsening of precipitates at elevated temperature; the strength decreases but thermal conductivity increases with precipitate coarsening. In order to develop new alloys with microstructures that lead to improved performance of cylinder heads, an effective compromise between thermal and mechanical properties needs to be achieved.

IV. SUMMARY AND CONCLUSIONS

In the present study, candidate cast aluminum alloys (206, 319, 356, A356, and A356 + 0.5Cu) for engine

cylinder heads were studied for mechanical and thermophysical property variation with heat treatment. The following are the salient conclusions of this investigation:

- The Al-Si alloys achieved peak-aged condition (T6) after 5 hours of heat treatment at their respective aging temperature. The higher aging temperature of 513 K (240 °C) for 319 leads to an over-aged condition (T7), while the alloy 206 exists in under-aged condition although not far from peak-aged T6 condition after 5 hours aging at 463 K (190 °C).
- In as-aged condition, the alloy 206 shows the highest, the alloy 319 intermediate, and three Al-Si alloys, the lowest hardness at room temperature. Size, number density, and other characteristics of the nano-scale precipitates formed during the aging treatment were found to determine the hardness/strength variation with alloy chemistry.
- Prolonged heat treatment causes a drastic drop in the mechanical response (hardness) for all the alloys due to significant coarsening of the strengthening precipitates. The alloy 319 is least affected as it is over-aged and 206 the most since it is under-aged to begin with.
- Strength modeling quantitatively confirms the effect of the size, number density, interface coherency, etc., of nano-scale precipitates on determining the strength of the investigated alloys.
- Coherent GPI and θ'' precipitates being quite small in size are effective for strength increment in as-aged 206 by interfacial strengthening due to their high number density.
- The semi-coherent θ' precipitates in as-aged 319 contribute to the strength increment by Orowan looping, although not to the extent compared to the 206 alloy due to the coarse size and much lower number density.
- The semi-coherent β' precipitates also improve strength of the A356 alloy in as-aged condition by Orowan looping; their contribution supersedes that from the θ' precipitates in 319 because of the high number density and fine size.
- Coarsening of nano-scale precipitates on over-aging or pre-conditioning significantly decreases their contribution to the CRSS increment of the alloys, which can be realized considering a corresponding decrease in number density or precipitate aspect ratio in the strength modeling equations.
- Thermal conductivity of the alloys, in contrast to their strength, increases when precipitates coarsen at elevated temperature or on pre-conditioning.
- The alloy 206 with finer GPI and θ'' precipitates shows moderate thermal diffusivity due to high number density of phonon scattering centers and also possibly due to the mass difference between Al and Cu atoms. Thermal properties are inferior for the 319 alloy with coarse precipitates that are effective scattering centers while Al-Si alloys have high number density of β' precipitates that are not as effective scattering centers because of their rod-shaped morphology.

- Alloys with microstructures that can lead to an effective compromise between thermal and mechanical properties will lead to the highest performance cylinder heads.

REFERENCES

1. S. Roy, L.F. Allard, A. Rodriguez, T.R. Watkins, and A. Shyam: *Metall. Mater. Trans. A*, 2016, DOI:10.1007/s11661-017-3985-1.
2. A.J. Ardell: *Metallurgical Transactions A*, 1985, vol. 16, pp. 2131–65.
3. J.W. Martin: *Precipitation Hardening: Theory and Applications*, Elsevier Science, 2012.
4. T. Gladman: *Mater. Sci. Technol.*, 1999, vol. 15, pp. 30–36.
5. C. Laird and H.I. Aaronson: *Acta Metall.*, 1966, vol. 14, pp. 171–85.
6. R. Yoshimura, T.J. Konno, E. Abe, and K. Hiraga: *Acta Material.*, 2003, vol. 51, pp. 4251–66.
7. G.C. Weatherly and C.M. Sargent: *Philos. Mag.*, 1970, vol. 22, pp. 1049–61.
8. SP Ringer, K Hono, and T Sakurai: *Metall. Mater. Trans. A*, 1995, vol. 26, pp. 2207–17.
9. M. Karlík, A. Bigot, B. Jouffrey, P. Auger, S. Belliot: *Ultramicroscopy*, 2004, vol. 98, pp. 219–30.
10. A. Biswas, D.J. Siegel, C. Wolverton, and D.N. Seidman: *Acta Material.*, 2011, vol. 59, pp. 6187–6204.
11. V. Fallah, A. Korinek, N. Ofori-Opoku, N. Provatas, and S. Esmaeili: *Acta Material.*, 2013, vol. 61, pp. 6372–86.
12. D. Vaughan and J.M. Silcock, *Phys. Stat. Solidi (b)*, 1967, vol. 20, pp. 725–36.
13. S.F. Baumann and D.B. Williams: *Scripta Metall.*, 1984, vol. 18, pp. 611–16.
14. S.Y. Hu, M.I. Baskes, M. Stan, and L.Q. Chen: *Acta Material.*, 2006, vol. 54, pp. 4699–4707.
15. L. Bourgeois, C. Dwyer, M. Weyland, J.-F. Nie, and B.C. Muddle: *Acta Material.*, 2011, vol. 59, pp. 7043–50.
16. L. Bourgeois, C. Dwyer, M. Weyland, J.-F. Nie, and B.C. Muddle: *Acta Material.*, 2012, vol. 60, pp. 633–44.

17. C. Wolverton: *Philos. Mag. Lett.*, 1999, vol. 79, pp. 683–90.
18. C. Wolverton and V. Ozoliņš: *Phys. Rev. Lett.*, 2001, vol. 86, pp. 5518–21.
19. V. Vaithyanathan, C. Wolverton, and L.Q. Chen: *Acta Material.*, 2004, vol. 52, pp. 2973–87.
20. J.D. Boyd and R.B. Nicholson: *Acta Metall.*, 1971, vol. 19, pp. 1379–91.
21. P. Merle and F. Fouquet: *Acta Metall.*, 1981, vol. 29, pp. 1919–27.
22. J.F. Nie and B.C. Muddle: *J. Phase Equilib.*, 1998, vol. 19, pp. 543–51.
23. J.F. Nie and B.C. Muddle: *Acta Materialia*, 2008, vol. 56, pp. 3490–3501.
24. J. da Costa Teixeira, L. Bourgeois, C.W. Sinclair, and C.R. Hutchinson: *Acta Materialia*, 2009, vol. 57, pp. 6075–89.
25. A.W. Zhu, J. Chen, and E.A. Starke, Jr: *Acta Materialia*, 2000, vol. 48, pp. 2239–46.
26. R.X. Li, R.D. Li, Y.H. Zhao, L.Z. He, C.X. Li, H.R. Guan, and Z.Q. Hu: *Mater. Lett.*, 2004, vol. 58, pp. 2096–2101.
27. D. Ovono Ovono, I. Guillot, and D. Massinon: *Scripta Material.*, 2006, vol. 55, pp. 259–62.
28. P. Ouellet and F.H. Samuel: *J. Mater. Sci.*, 1999, vol. 34, pp. 4671–97.
29. F.J. Tavitas-Medrano, A.M.A. Mohamed, J.E. Gruzleski, F.H. Samuel, and H.W. Doty: *Journal of Materials Science*, 2009, vol. 45, pp. 641–51.
30. S.C. Weakley-Bollin, W. Donlon, W. Donlon, C. Wolverton, J.E. Allison, and J.W. Jones: *Metall. Mater. Trans. A*, 2004, vol. 35, pp. 2407–18.
31. K. Liu, X. Cao, and X.-G. Chen: *Metall. Mater. Trans. B*, 2015, vol. 46, pp. 1566–75.
32. W.W. Zhang, B. Lin, D.T. Zhang, and Y.Y. Li: *Mater. Des.*, 2013, vol. 52, pp. 225–33.
33. Y. Sui, Q. Wang, T. Liu, B. Ye, H. Jiang, and W. Ding: *J. Alloys Compd.*, 2015, vol. 644, pp. 228–35.
34. S.K. Shaha, F. Czerwinski, W. Kasprzak, J. Friedman, and D.L. Chen: *Metall. Mater. Trans. A*, 2016, vol. 47, pp. 2396–2409.
35. R. Ahmad and M.B.A. Asmael: *Journal of Materials Engineering and Performance*, 2016, vol. 25, pp. 2799–2813.
36. S.K. Shaha, F. Czerwinski, W. Kasprzak, J. Friedman, and D.L. Chen: *Metall. Mater. Trans. A*, 2015, vol. 46, pp. 3063–78.
37. L. Tao, Y. Pan, W. Ji-li, Shi.-wen. Tao, and Yu. Chen: *Int. J. Miner. Metall. Mater.*, 2015, vol. 22, pp. 405–10.
38. H. Yang, S. Ji, and Z. Fan: *Mater. Des.*, 2015, vol. 85, pp. 823–32.
39. M.F. Ibrahim, A.M. Samuel, H.W. Doty, and F.H. Samuel: *Int. J. Metalcast.*, 2016, pp. 1–13.
40. S.K. Chaudhury, D. Apelian, P. Meyer, D. Massinon, and J. Morichon: *Metall. Mater. Trans. A*, 2015, vol. 46, pp. 3276–86.
41. H. Yang, S. Ji, W. Yang, Y. Wang, and Z. Fan: *Mater. Sci. Eng. A*, 2015, vol. 642, pp. 340–50.
42. Y. Sui, Q. Wang, G. Wang, and T. Liu: *J. Alloys Compd.*, 2015, vol. 622, pp. 572–79.
43. S.C. Wang and M.J. Starink: *Int. Mater. Rev.*, 2005, vol. 50, pp. 193–215.
44. K. Teichmann, C.D. Marioara, S.J. Andersen, and K. Marthinsen: *Mater. Charact.*, 2013, vol. 75, pp. 1–7.
45. G.A. Edwards, K. Stiller, G.L. Dunlop, and M.J. Couper: *Acta Material.*, 1998, vol. 46, pp. 3893–3904.
46. J.Y. Yao, D.A. Graham, B. Rinderer, and M.J. Couper: *Micron*, 2001, vol. 32, pp. 865–70.
47. K. Matsuda, S. Ikeno, K. Gamada, K. Fujii, Y. Uetani, T. Sato, and A. Kamio: *Metall. Mater. Trans. A*, 1998, vol. 29, pp. 1161–67.
48. D.G. Eskin: *J. Mater. Sci.*, 2003, vol. 38, pp. 279–90.
49. V. Fallah, B. Langelier, N. Ofori-Opoku, B. Raeisinia, N. Provatas, and S. Esmaeili: *Acta Material.*, 2016, vol. 103, pp. 290–300.
50. Q.G. Wang and C.J. Davidson: *J. Mater. Sci.*, 2001, vol. 36, pp. 739–50.
51. W. Kasprzak, H. Kurita, G. Birsan, and B.S. Amirkhiz: *Mater. Des.*, 2016, vol. 103, pp. 365–76.
52. P. Zhang, Z. Li, B. Liu, and W. Ding: *Mater. Sci. Eng. A*, 2016, vol. 661, pp. 198–210.
53. K.A. Abuhasel, M.F. Ibrahim, E.M. Elgallad, and F.H. Samuel: *Mater. Des.*, 2016, vol. 91, pp. 388–97.
54. B. Wan, W. Chen, L. Liu, X. Cao, L. Zhou, and F. Zhiqiang: *Mater. Sci. Eng. A*, 2016, vol. 666, pp. 165–75.
55. M. Zamani and S. Seifeddine: *Int. J. Metalcast.*, 2016, pp. 1–9.
56. C.H. Caceres, C.J. Davidson, J.R. Griffiths, and Q.G. Wang: *Metall. Mater. Trans. A*, 1999, vol. 30, pp. 2611–18.
57. E. Sjölander and S. Seifeddine: *J. Mater. Process. Technol.*, 2010, vol. 210, pp. 1249–59.
58. R.A. Siddiqui, H.A. Abdullah, and K.R. Al-Belushi: *J. Mater. Process. Technol.*, 2000, vol. 102, pp. 234–40.
59. M. Abdulwahab, I.A. Madugu, S.A. Yaro, S.B. Hassan, and A.P.I. Popoola: *Materials & Design*, 2011, vol. 32, pp. 1159–66.
60. H. Möller, G. Govender, and W.E. Stumpf: *Int. J. Cast Metals Res.*, 2007, vol. 20, pp. 340–46.
61. D.K. Dwivedi, R. Sharma, and A. Kumar: *Int. J. Cast Metals Res.*, 2006, vol. 19, pp. 275–82.
62. S. Esmaeili, X. Wang, D.J. Lloyd, and W.J. Poole: *Metall. Mater. Trans. A*, 2003, vol. 34, pp. 751–63.
63. A.K. Gupta, D.J. Lloyd, and S.A. Court: *Mater. Sci. Eng. A*, 2001, vol. 316, pp. 11–17.
64. O.R. Myhr, Ø. Grong, and S.J. Andersen: *Acta Material.*, 2001, vol. 49, pp. 65–75.
65. P.A. Rometsch and G.B. Schaffer: *Mater. Sci. Eng. A*, 2002, vol. 325, pp. 424–34.
66. W.A. Knox: *Ultramicroscopy*, 1976, vol. 1, pp. 175–80.
67. S.E. Landwehr, G.E. Hilmas, W.G. Fahrenholtz, I.G. Talmy, and H. Wang: *Mater. Chem. Phys.*, 2009, vol. 115, pp. 690–95.
68. N.F. Mott and F.R.N. Nabarro: *Proc. Phys. Soc.*, 1940, vol. 52, p. 86.
69. W. Kasprzak, F. Czerwinski, M. Niewczas, and D.L. Chen: *J. Mater. Eng. Perform.*, 2015, vol. 24, pp. 1365–78.
70. L. Ding, Z. Jia, Y. Liu, Y. Weng, and Q. Liu: *J. Alloys Compd.*, 2016, vol. 688A, pp. 362–67.
71. V.M.J. Sharma, K.S. Kumar, B.N. Rao, and S.D. Pathak: *Metall. Mater. Trans. A*, 2009, vol. 40, pp. 3186–95.
72. M.E. Fine: *Metall. Trans. A*, 1975, vol. 6, pp. 625–30.
73. C. Booth-Morrison, D.C. Dunand, and D.N. Seidman: *Acta Material.*, 2011, vol. 59, pp. 7029–42.
74. C.B. Fuller, D.N. Seidman, and D.C. Dunand: *Acta Material.*, 2003, vol. 51, pp. 4803–14.
75. M. Murayama, K. Hono, W.F. Miao, and D.E. Laughlin: *Metall. Mater. Trans. AA*, 2001, vol. 32, pp. 239–46.
76. M. Murayama and K. Hono: *Acta Materialia*, 1999, vol. 47, pp. 1537–48.
77. S. Esmaeili, D.J. Lloyd, and W.J. Poole: *Acta Materialia*, 2003, vol. 51, pp. 3467–81.
78. Ø. Ryen, B. Holmedal, O. Nijs, E. Nes, E. Sjölander, and H.-E. Ekström: *Metall. Mater. Trans. A*, 2006, vol. 37, pp. 1999–2006.
79. J. da Costa Teixeira, D.G. Cram, L. Bourgeois, T.J. Bastow, A.J. Hill, and C.R. Hutchinson: *Acta Material.*, 2008, vol. 56, pp. 6109–22.
80. M. Song: *Mater. Sci. Eng. A*, 2007, vol. 443, pp. 172–77.
81. O.R. Myhr, Ø. Grong, H.G. Fjær, and C.D. Marioara: *Acta Materialia*, 2004, vol. 52, pp. 4997–5008.
82. K.E. Knipling, D.C. Dunand, and D.N. Seidman: *Acta Material.*, 2008, vol. 56, pp. 1182–95.
83. K.E. Knipling, D.C. Dunand, and D.N. Seidman: *Acta Material.*, 2008, vol. 56, pp. 114–27.
84. E.A. Marquis, D.N. Seidman, and D.C. Dunand: *Acta Material.*, 2003, vol. 51, pp. 285–87.
85. A.W. Zhu, A. Csontos, and E.A. Starke, Jr: *Acta Material.*, 1999, vol. 47, pp. 1713–21.
86. A. de Vaucorbeil, W.J. Poole, and C.W. Sinclair: *Mater. Sci. Eng. A*, 2013, vol. 582, pp. 147–54.
87. G. Liu, G.J. Zhang, X.D. Ding, J. Sun, and K.H. Chen: *Mater. Sci. Eng. A*, 2003, vol. 344, pp. 113–24.
88. G. Grimvall: *Thermophysical Properties of Materials*, Elsevier Science, 1999.
89. T.M. Tritt: *Thermal Conductivity: Theory, Properties, and Applications*, Springer, US, 2006.
90. L. Han, N. Van Nong, W. Zhang, L.T. Hung, T. Holgate, K. Tashiro, N. Pryds, and S. Linderoth: *RSC Adv.*, 2014, vol. 4, pp. 12353–61.
91. J.M. Pelletier, G. Vigier, J. Merlin, P. Merle, F. Fouquet, and R. Borrelly: *Acta Metall.*, 1984, vol. 32, pp. 1069–78.

92. S. Gorsse, P. Bellanger, Y. Brechet, E. Sellier, A. Umarji, U. Ail, and R. Decourt: *Acta Material.*, 2011, vol. 59, pp. 7425–37.
93. J. Callaway and H.C. von Baeyer: *Phys. Rev.*, 1960, vol. 120, pp. 1149–54.
94. A.M.B. Collieu and D.J. Powney: *The Mechanical and Thermal Properties of Materials*, Crane Russak, 1973.
95. B.P. Bhardwaj: *The Complete Book on Production of Automobile Components & Allied Products*, NIIR Project Consultancy Services, 2014.